BIBTEX Citation Entry

```
@article{ZhuJNNFM18,
 author = {Zhu, Lu and Schrobsdorff, Hecke
        and Schneider, Tobias M. and Xi,
        Li},
 title = {{Distinct transition in flow
        statistics and vortex dynamics
        between low- and high-extent
        turbulent drag reduction in
        polymer fluids}},
 journal= {Journal of Non-Newtonian Fluid
        Mechanics},
 volume = {262},
 pages  = {115-130},
 year   = {2018},
}
```
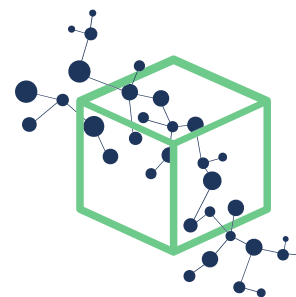
brought to you by the
XI RESEARCH GROUP at McMaster University

— www.XIRESEARCH.org —

Principle Investigator:
Li Xi 奚力
Email: li@xiresearch.org

https://twitter.com/xiresearchgroup
https://linkedin.com/company/xiresearch/
https://researchgate.net/profile/Li_Xi16
https://mendeley.com/profiles/li-xi11/

Distinct transition in flow statistics and vortex dynamics between low- and high-extent turbulent drag reduction in polymer fluids

Lu Zhu[a], Hecke Schrobsdorff[b], Tobias M. Schneider[c,d], Li Xi[a,d,*]

[a]*Department of Chemical Engineering, McMaster University, Hamilton, Ontario L8S 4L7, Canada*
[b]*Max Planck Institute for Dynamics and Self-Organization, Am Fassberg 17, 37077 Göttingen, Germany*
[c]*Emergent Complexity in Physical Systems Laboratory (ECPS), École Polytechnique Fédérale de Lausanne, Switzerland*
[d]*Kavli Institute for Theoretical Physics (KITP), University of California, Santa Barbara, California 93106-4030, U.S.A*

Abstract

Flexible polymer additives are known to reduce the energy dissipation and friction drag in turbulent flows. As the fluid elasticity increases, the flow undergoes several stages of transitions. Much attention in the area has been focused on the onset of drag reduction (DR) and the eventual convergence to the maximum drag reduction (MDR) asymptote. Between the onset and MDR, recent experimental and numerical observations prompted the need to further distinguish the low- and high-extent drag reduction (LDR and HDR). Fundamental knowledge of this transition will be important for understanding turbulent dynamics in the presence of polymers, as well as for inspiring new flow control strategies for efficient friction reduction. We use direct numerical simulation (DNS) to explore all these transitions in the parameter space and, in particular, demonstrate that the LDR-HDR transition is not merely a quantitative effect of the level of drag reduction, but a qualitative transition into a different stage of turbulence. A number of sharp changes in flow statistics are found to accompany the transition and at HDR, turbulence becomes localized with vortices forming clusters. These

---

*Corresponding author
Email address:* `xili@mcmaster.ca` (Li Xi)

observations suggest that polymer-induced drag reduction follows two distinct stages. The first starts at the onset of drag reduction, where the coil-stretch transition of polymers causes an overall suppression of turbulent fluctuations. The second starts at the LDR-HDR transition, where flow statistics become fundamentally changed in the log-law layer and turbulence localization is observed. A mechanism is then proposed for the latter based on the changing vortex regeneration dynamics between LDR and HDR.

1. Introduction

The phenomenon of turbulent drag reduction (DR) caused by polymer additives is widely known and has been studied extensively in the literature [1, 2, 3]. As a small quantity of polymers is added to a Newtonian liquid, turbulent structures are modified. The resulting friction drag reduction, measured by

$$\text{DR}\% \equiv \frac{C_{\text{f,s}} - C_{\text{f}}}{C_{\text{f,s}}} \tag{1}$$

($C_{\text{f,s}}$ and C_{f} are the friction factors of the pure solvent and polymer solution, respectively), can reach up to 80%. As a result, the mean flow rate under the same pressure drop increases which considerably enhances the fluid transportation efficiency. Understanding of this phenomenon has significant practical implications for the development of mechanical flow control schemes and has thus gained significant attention since the 1940s.

In viscoelastic fluids, polymer-induced elasticity is measured by the Weissenberg number $\text{Wi} = \lambda \dot{\gamma}$, which is defined as the product of the polymer relaxation time λ and the shear rate $\dot{\gamma}$ of the flow. Below a critical magnitude of Wi, the mean flow is statistically indistinguishable from that of Newtonian turbulence: in most of the boundary layer, both follow the same Prandtl-von Kármán (PvK) log law [4]
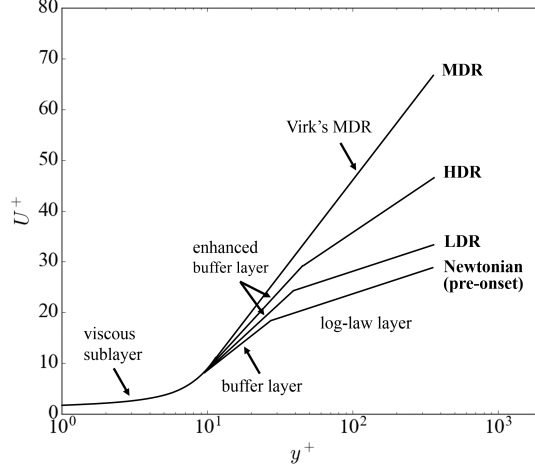
2

Figure 1: Schematic of mean velocity profiles (mean streamwise velocity as a function of the distance from the wall) at different stages of DR.

$$U^+ = 2.5y^+ + 5.5 \qquad (2)$$

where the superscript "+" indicates quantities in turbulent inner scales: i.e. velocities and lengths are scaled by the friction velocity and viscous length scale or "wall unit" (see definitions in Section 2), respectively. The onset of DR typically occurs at $\mathrm{Wi}_{\mathrm{onset}} = O(10)$ [5, 6, 7, 8]. Further raising Wi leads to increasing levels of DR (see Figure 1), which eventually saturate and approach an asymptotic upper bound. Rather surprisingly, this maximum drag reduction (MDR) asymptote is found to be insensitive to the rheological properties of the polymer solution [1].

The original theory of Virk [1] postulates that polymer effects concentrate in the buffer layer, corresponding to $5 \lesssim y^+ \lesssim 30$ in Newtonian turbulence (right below the log-law layer) [9]. Increasing Wi leads to a thicker buffer layer, now termed the "elastic sublayer" to reflect the polymer effects, but the log law layer remains unaffected with the same slope and only a larger intercept (Figure 1). The elastic sublayer keeps on expanding with increasing Wi until

3

MDR is reached where it occupies the whole channel.

Despite the intellectual appeal of its conceptual simplicity, this elastic sublayer theory was later proven oversimplified. Experiments by Warholic et al. [10] revealed that the PvK-like log law is only preserved for low-extent DR (LDR) ($\lesssim$ 35% in that study) and for high-extend DR (HDR), the slope of the mean velocity profile in a linear-log plot is ostensibly higher than the PvK magnitude (Figure 1). This was further confirmed by a number of experimental and numerical studies [5, 7, 8, 11, 12, 13]. Although often associated with the quantitative magnitude of DR% in the literature, emerging evidences have suggested that the LDR-HDR transition is indeed a qualitative change in the turbulent dynamics. A recent analysis by White et al. [14] showed that at HDR U^+ does not even strictly follow a logarithmic dependence. In addition, for minimal flow units (MFUs) and one low Re, Xi and Graham [7] showed that this change in the shape of the $U^+(y^+)$ profile can occur at DR% as low as $\approx$ 15: DR% > 30 is not required for HDR behaviors. Beyond the mean velocity profile, changes between LDR and HDR in other quantities are much less documented. Major observations (in the aforementioned studies) at HDR include significantly reduced Reynolds shear stress and smooth flow field patterns with longer streamwise correlation, although direct connections with the LDR-HDR transition still need to be established.

MDR is arguably the crown jewel of this field, whose curious nature remains puzzling in many respects. However, the hitherto over-shadowed problem of LDR-HDR transition certainly deserves attention in its own right. For one thing, it has significant practical implication in the area of turbulence control. Existing mechanical (non-additive-based) flow control techniques pale in comparison with polymer-induced DR: both the DR% achieved by these techniques and the shape of the $U^+(y^+)$ profile are only comparable to LDR in polymer fluids [15] – understanding the turbulent dynamics of HDR will be pivotal to break this ceiling. Meanwhile, the fundamental significance also should not be overlooked. Despite the ongoing debate between viscous vs elastic mechanisms [16, 17], it has been generally accepted that DR is caused by the polymer-turbulence interaction

4

and the resulting suppression of vortical structures [18, 19, 20, 21]. This effect kicks in at the coil-stretch transition of the polymers [8] and corresponds to the onset of DR. The additional LDR-HDR transition at Wi distinctly higher than the onset suggests that there is another change in the underlying polymer-turbulence dynamics that we do not as yet understand: i.e. DR with increasing polymer elasticity is a two stage process with a first mechanism being triggered at the onset and a second mechanism at the LDR-HDR transition. The change in the $U^+(y^+)$ profile suggests that the first mechanism mainly acts in the buffer layer whereas the second one extends to the log-law layer.

In the recent framework by Xi and Graham [22], turbulent dynamics in MFUs is classified into two phases: regular strong turbulence that dominates the Newtonian flow is termed active turbulence and weak nearly two-dimensional turbulent state is termed hibernating turbulence. The latter occurs in Newtonian flow as well – which was confirmed in experiments [23] and believed to be intermittent visits towards the laminar-turbulent edge state [24, 25] – with very low frequency but becomes unmasked at high Wi. Its remarkable resemblance to MDR prompts the hypothesis that MDR is an asymptotic state where hibernating turbulence becomes the statistical norm. Taking an ergodic view of turbulence and neglecting the long-range spatial correlation, the temporal intermittency in MFUs (between active and hibernating periods) should reflect the spatial intermittency in extended flow domains. This was investigated recently by Wang et al. [26] who showed that flow-field patches corresponding to active and hibernating regions can be clearly identified in a large domain and the total area of hibernating patches increases as the flow converges to MDR. Interestingly, in MFUs and at least one low Re, the Wi where hibernation frequency starts to ramp up seems to coincide with that of the LDR-HDR transition [27]. If HDR is indeed triggered by the unmasking of hibernating turbulence, that would perfectly explain the change in the shape of the $U^+(y^+)$ profile, as conditional average studies have revealed that hibernating turbulence has a drastically steeper $U^+(y^+)$ profile than active turbulence [26, 27]. This link, however, has not been tested in larger domains nor for more than one Re. As we will show

later, the correlation between vortex dynamics in different regions turns out to be important for understanding HDR, which was not considered in this MFU framework.

The purpose of this study is first to systematically investigate the differences between LDR and HDR in an extensive flow domain (compared with MFU) by densely sampling the parameter space. In particular, at each Re and in both LDR and HDR regimes, multiple points need to be included to establish the LDR-HDR transition as a qualitative one. A new mechanism will be proposed for the changing vortex dynamics underlying the transition. The paper is organized as follows. After introducing our simulation approach in Section 2, changes in flow statistics at the LDR-HDR transition will first be summarized in Section 3.1. We will then study and quantify the transitions in flow structure (Section 3.2). Our new mechanism for the changing vortex dynamics at HDR is proposed in Section 3.3.

2. Formulation and numerical details

Direct Numerical Simulation (DNS) of the governing equations in a plane Poiseuille geometry is performed following the standard procedure first introduced by Sureshkumar et al. [28]. The geometry of the simulation domain is shown in Figure 2(a). The flow is driven by a fixed streamwise pressure gradient orientated in the x-direction. The no-slip boundary condition is applied to the walls (y-direction) and the periodic boundary condition is applied to both the streamwise (x-direction) and spanwise (z-direction) boundaries. The periods are denoted by L_x and L_z, respectively. By default, all variables are nondimensionalized by turbulent outer units: i.e., lengths are scaled by the half-channel height l, velocities by the laminar center-line velocity U_c, time by l/U_c, and pressure by ρU_c^2 (ρ is the total density of the fluid). Meanwhile, near-wall quantities are often represented in inner scales: velocities scaled by the friction velocity $u_\tau \equiv \sqrt{\tau_w/\rho}$ and lengths by the viscous length scale $\delta_v \equiv \eta/\rho u_\tau$, where τ_w is the mean wall shear stress and η is the solution viscosity. Then for $\mathrm{Re} \equiv \rho U_c l/\eta$,
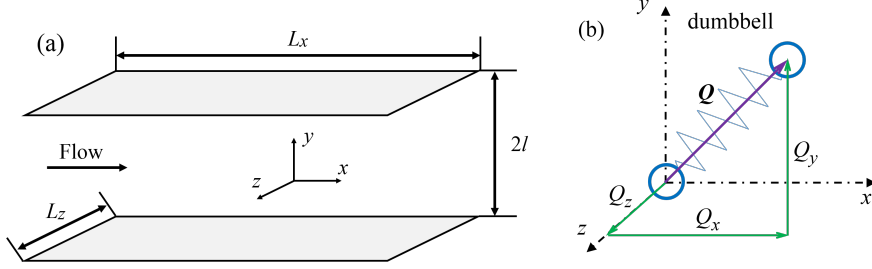
Figure 2: Schematics of the (a) flow geometry and (b) FENE-P dumbbell

the friction Reynolds number $\mathrm{Re}_\tau \equiv \rho u_\tau l / \eta = \sqrt{2\mathrm{Re}}$. The y coordinate in the inner scale y^+ ranges from 0 at the wall to $y^+_{\mathrm{CL}} = \mathrm{Re}_\tau$ at the channel center-line.

The momentum and mass balance equations are

$$\frac{\partial \boldsymbol{v}}{\partial t} + \boldsymbol{v} \cdot \boldsymbol{\nabla} \boldsymbol{v} = -\boldsymbol{\nabla} p + \frac{\beta}{\mathrm{Re}} \nabla^2 \boldsymbol{v} + \frac{2\,(1-\beta)}{\mathrm{ReWi}} \left(\boldsymbol{\nabla} \cdot \boldsymbol{\tau}_p\right), \qquad (3)$$

$$\boldsymbol{\nabla} \cdot \boldsymbol{v} = 0. \qquad (4)$$

where the Weissenberg number Wi is the product of polymer relaxation time λ and the mean wall shear rate, i.e., $\mathrm{Wi} \equiv \lambda U_c / l$ and $\beta \equiv \eta_\mathrm{s} / \eta$ is the ratio of the solvent viscosity to the total viscosity. The last term on the right-hand-side of Equation (3) accounts for the polymer effect, where $\boldsymbol{\tau}_p$ is the polymer stress tensor. It is calculated with the FENE-P constitutive equation [29]

$$\frac{\boldsymbol{\alpha}}{1 - \frac{\mathrm{tr}(\boldsymbol{\alpha})}{b}} + \frac{\mathrm{Wi}}{2} \left(\frac{\partial \boldsymbol{\alpha}}{\partial t} + \boldsymbol{v} \cdot \boldsymbol{\nabla} \boldsymbol{\alpha} - \boldsymbol{\alpha} \cdot \boldsymbol{\nabla} \boldsymbol{v} - (\boldsymbol{\alpha} \cdot \boldsymbol{\nabla} \boldsymbol{v})^{\mathrm{T}} \right) = \frac{b\boldsymbol{\delta}}{b+2}, \qquad (5)$$

$$\boldsymbol{\tau}_p = \frac{b+5}{b} \left(\frac{\boldsymbol{\alpha}}{1 - \frac{\mathrm{tr}(\boldsymbol{\alpha})}{b}} - \left(1 - \frac{2}{b+2}\right)\boldsymbol{\delta} \right). \qquad (6)$$

The FENE-P model treats polymer molecules as finitely extensible nonlinear elastic (FENE) dumbbells, as shown in Figure 2(b). The polymer conformation tensor is defined as $\boldsymbol{\alpha} \equiv \langle \boldsymbol{Q}\boldsymbol{Q} \rangle$, where $\boldsymbol{Q}$ donates the end-to-end vector of the dumbbell. The length of the dumbbells is constrained by the maximum extensibility parameter b: i.e., $\max(\mathrm{tr}(\boldsymbol{\alpha})) \leq b$.

7

Re	Re_τ	δ_t	L_x^+	L_z^+	δ_x^+	δ_z^+
3711	86.15	0.01	4000	800	9.09	5.44
7423	121.84	0.01	4000	800	9.09	5.44
14845	172.31	0.01	4000	800	9.09	5.44

Re	N_y	$\delta_{y,\mathrm{min}}^+$	$\delta_{y,\mathrm{max}}^+$	Sc	1/ScRe
3711	97	0.046	2.81	0.5	5.39×10^{-4}
7423	127	0.038	3.03	0.3	4.49×10^{-4}
14845	195	0.022	2.79	0.3	2.25×10^{-4}

Table 1: Numerical settings for production runs.

No.	Re_τ	Wi	Sc	$1/(\mathrm{ScRe})$	$L_x^+ \times L_z^+$	$N_x \times N_y \times N_z$
1	86.15	64	0.3	8.98×10^{-4}	4000×800	$256 \times 59 \times 87$
2	86.15	64	0.5	5.39×10^{-4}	4000×800	$440 \times 97 \times 147$
3	86.15	64	0.75	3.59×10^{-4}	4000×800	$640 \times 145 \times 221$

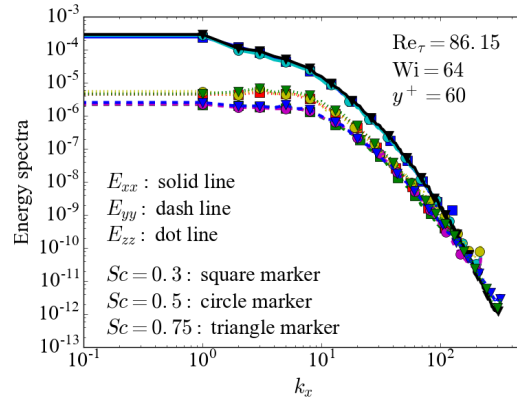Table 2: Settings of the validation tests.

Figure 3: Three components of the one-dimensional energy spectra against the spanwise wave number at $y^+ = 60$.

All variables are discretized with a Fourier-Chebyshev-Fourier pseudo-spectral scheme. The grid size in the x direction is $\delta_x^+ = 9.09$ and that in the z direction is $\delta_z^+ = 5.44$; the number of grid points in the y direction is 97, 127, and 195 for $\text{Re}_\tau = 86.15$, 121.84, and 172.31, respectively. For the time integration, we adopt a third-order semi-implicit backward-differentiation/Adams-Bashforth scheme [30], and the time step is chosen to be $\delta_t = 0.01$. Numerical settings used in production runs are listed in Table 1. An artificial diffusion term $1/(\text{ScRe})\nabla^2\boldsymbol{\alpha}$ is added to the right-hand side of Equation (5) with the Schmidt number $\text{Sc} = 0.5$ for $\text{Re}_\tau = 86.15$ and 0.3 for $\text{Re}_\tau = 121.84$ and 172.31. This term is required for the numerical stability of the pseudo-spectral method used here and it has been established in the literature that a numerical diffusivity of $O(0.01)$ does not significantly impact the results [8, 11, 28, 31, 32]. The magnitudes of diffusivity $1/\text{ScRe}$ used in this study are all at $O(10^{-4})$ (Table 1). According to Sureshkumar et al. [28], Sureshkumar and Beris [31], when the numerical diffusivity decreases (by increasing Sc) linearly with the grid size, the solution converges to that of the original equation. This convergence is validated here for a high-Wi case with proportionally varying resolution and numerical diffusivity as listed in Table 2. As an example, we present the streamwise one-dimensional energy spectra of all three velocity components – defined as

$$E_{ii}(k_x) = \int_{k_z} \hat{v}_i'^* \cdot \hat{v}_i' dk_z \qquad (7)$$

(where $i = x, y, z$ is the index for velocity components, "$\prime$" indicates the fluctuating component of the velocity field, $\hat{\cdot}$ indicates the Fourier transform, and "$*$" indicates the complex conjugate) – in Figure 3. For all cases, results from different resolutions and numerical diffusivity magnitudes well collapse onto one another, indicating that our choice of Sc is sufficient.

The numerical code used for this study is a custom MPI-parallelized code developed based on the C++ Channelflow package [33]. A Newtonian version of the code was earlier used for the DNS of Newtonian Poiseuille flow [34]; the code was then extended for viscoelastic simulation by integrating the original

9

algorithm of Xi and Graham [7].

3. Results and Discussion

Simulations in this study are all performed in the box size of $L_x^+ \times L_z^+ =$ 4000 × 800, which is well within the range considered to be an extended domain. A series of Wi at each of three different Re_τ (86.15, 121.84, and 172.31) are reported. These Re_τ values are closer to the critical magnitude $\mathrm{Re}_{\tau,\mathrm{crit}} \approx 45$ for the laminar-turbulent transition [35] than several recent high-Re viscoelastic turbulence DNS studies [8, 36]. This choice is deliberate. Previous research has clearly shown that all key stages of viscoelastic turbulence are observed in the near-transition regime [1, 7]: higher Re is not a necessary condition for the LDR-HDR transition. At lower Re, the turbulent dynamics is more tractable and also different stages of DR are contained in a smaller parameter-space region (see Figure 5), both bringing mechanistic understanding within reach. On the other hand, unlike most previous studies which focused on the direct comparison between one LDR and one HDR case, our attention is on the parametric dependence of the qualitative behaviours. This requires simulations at a larger number of parameter combinations and keeping the Re at this level reduces the computational cost per run. (Nevertheless, the computation is still substantial: for viscoelastic simulation at the highest $\mathrm{Re}_\tau = 172.31$ and running on 32 processors in parallel, the time-stepper proceeds by ≈ 7 time units per wall-clock hour; each data point, including both equilibration and production runs, requires 3500 time units, which takes more than 20 days on a state-of-the-art computing facility.) For the two lower Re, the full transition path from Newtonian to MDR is captured. For the highest Re, numerical instability starts to show up at Wi = 96. Instead of increasing the artificial diffusivity, we decided to exclude results at higher Wi since Wi = 96 is already well beyond the LDR-HDR transition. The rheological parameters b and β in all cases are fixed to be 5000 and 0.97, respectively. Time average results in this section are all calculated from 20 evenly-spaced snapshots within a total period of 1000 time
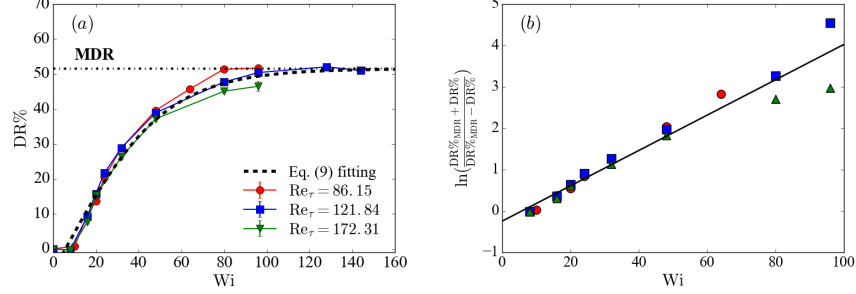
10

Figure 4: (a) dependence of the percentage of drag reduction (DR%) on Wi at $\mathrm{Re}_\tau = 86.15$, 121.84 and 172.31 and comparison with the empirical fitting using eq. (9); (b) linear regression plot using eq. (10) (data symbols are the same as those in panel (a)).

units, after the DNS solution has reached the statistical steady state.

3.1. Changes in flow statistics

In this section, statistical results are summarized and compared between LDR and HDR. In Figure 4, DR% as a function of Wi are plotted for three Reynolds numbers Re_τ: 86.15, 121.84 and 172.31. (DR% is defined in Equation (1) and the friction factor is defined as

$$C_f \equiv \frac{2\tau_w}{\rho U_{\mathrm{avg}}^2} \tag{8}$$

where U_{avg} is the volume average streamwise velocity.) As expected, DR% of all Re increases with Wi. Interestingly, profiles of three Re nearly overlap until they get close to the asymptotic plateau. This suggests that the quantitative dependence of DR% on Wi can be approximated by the same empirical correlation, as also reported by Housiadas and Beris [37], Owolabi et al. [38]. We adopt the same formula used by Housiadas and Beris [37]

$$\frac{\mathrm{DR}\%}{\mathrm{DR}\%_{\mathrm{MDR}}} = \begin{cases} 0 & (\mathrm{Wi} < \mathrm{Wi}_{\mathrm{onset}}) \\ 1 - \dfrac{2}{1 + \exp\left(\frac{\mathrm{Wi} - \mathrm{Wi}_{\mathrm{onset}}}{\mathscr{W}}\right)} & (\mathrm{Wi} \geq \mathrm{Wi}_{\mathrm{onset}}) \end{cases} \tag{9}$$

which models a smooth monotonic increase from DR% = 0 at $\mathrm{Wi}_{\mathrm{onset}}$ to DR% = DR%$_{\mathrm{MDR}}$ as Wi $\to \infty$; parameter $\mathscr{W}$ adjusts the profile steepness. We set

11

DR%$_{\text{MDR}}$ = 51.5% which is the average DR% value of our MDR data points. Equation (9) is then rearranged to

$$\ln\left(\frac{\text{DR\%}_{\text{MDR}} + \text{DR\%}}{\text{DR\%}_{\text{MDR}} - \text{DR\%}}\right) = \frac{\text{Wi}}{\mathscr{W}} - \frac{\text{Wi}_{\text{onset}}}{\mathscr{W}} \qquad (10)$$

from which $\mathscr{W}$ and Wi$_{\text{onset}}$ can be determined with linear regression. The regression line from all our LDR and HDR data points is shown in Figure 4(b). The data points remain close to the linear line until very high Wi (> 60), indicating that Equation (9) offers satisfactory correlation except in the regime near MDR (also seen in Figure 4(a)). Parameters obtained from the regression – Wi$_{\text{onset}}$ = 5.76 and $\mathscr{W}$ = 23.41 – are very close to the values estimated by Housiadas and Beris [37] (Wi$_{\text{onset}}$ = 6 and $\mathscr{W}$ = 25). The agreement is expected since Housiadas and Beris [37]'s relation was also based on DNS data over a broad range of Re$_\tau$ (which covers our Re$_\tau$ magnitudes). Note that Equation (9) is simply a more general form of the Owolabi et al. [38] model: it reduces to the latter when Wi$_{\text{onset}}$ = 1/2 and $\mathscr{W}$ = 1. Owolabi et al. [38]'s Wi$_{\text{onset}}$ was much lower because there is no one-to-one mapping between the definitions of Wi in experiments and in DNS. Even after this difference is corrected for, fitting of our data to the Owolabi et al. [38]'s form is less successful: the additional steepness parameter $\mathscr{W}$ in eq. (9) is necessary.

Also noteworthy is that the LDR-HDR transition, which occurs at around DR% = 20% (shown later in Figure 9), is not reflected as any discernible change of trend in DR%. For the two lower Re$_\tau$ where high Wi results are available, DR% eventually saturates to an asymptotic upper limit. In its literal interpretation, MDR is the limit where DR% saturates with polymer elasticity. We will therefore refer to this limit as MDR in this paper. Further increasing the Wi causes the flow to laminarize. Experimentally, MDR should be a self-sustaining turbulent state where laminarization is avoided. However, re-laminarization at Wi is often observed in simulation studies [5, 7]. There are several possible causes for this discrepancy, including the lower Re and limited domain size used in simulations. Deterioration of numerical accuracy due to the artificial diffusion may also play a role at this level of Wi [12]. Nevertheless, the LDR-HDR tran-
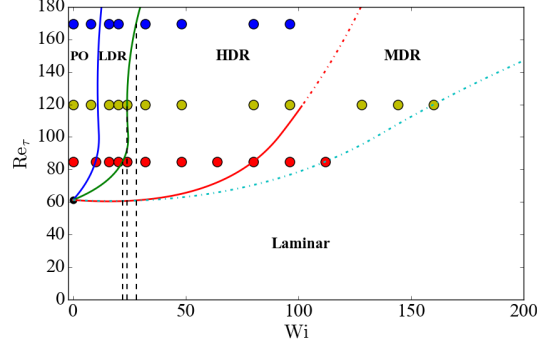
12

Figure 5: Multi-stage transitions of DR behaviours in the Re-Wi parameter space. Transition boundaries are drawn according to the B-spline interpolation between the critical Wi of the transitions at different Re_τ. Vertical dashed lines indicate the LDR-HDR transition for each Re_τ.

sition studied here occurs at much lower Wi and none of the major conclusions of this study should be affected.

Simulation points reported in this study are summarized in a Re-Wi parameter space in Figure 5, which is divided into four stages of DR behaviours: pre-onset (P.O.), LDR, HDR, and MDR. In the current domain, $Re_\tau = 61.28$ is the smallest Re to observe sustained turbulence, where introducing polymers immediately leads to laminarization. At the higher Re, the full transition path from Newtonian turbulence to MDR is observed, resonating with the experimental observation that qualitative transitions in viscoelastic turbulence extends all the way down to the laminar-turbulent transition regime. Critical Wi's for the transitions increases with Re_τ, leading to a wider range of Wi being occupied by each stage. Convergence to MDR occurs at Wi = 80 for $Re_\tau = 86.15$ and Wi = 128 for $Re_\tau = 121.84$. Variation in the onset Wi is almost negligible and a $Wi_{onset} \approx 10$ is observed for all cases. The critical Wi for the LDR-HDR transition is 22, 24, and 28 for $Re_\tau = 86.15$, 121.84, and 172.31, respectively.

Current results of $Re_\tau = 86.15$ are compared with the MFU simulation of Xi and Graham [7]. The $Re_\tau = 84.85$ of that study is very close to the current value and the rheological properties (i.e. β and b) are the same. The only different
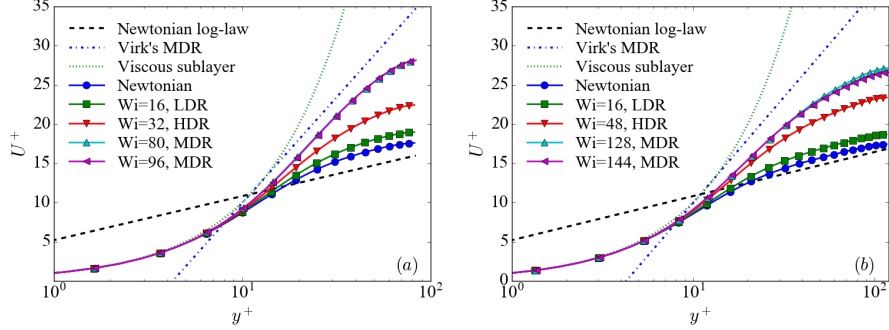
Figure 6: Mean velocity profiles (U^+ vesus y^+) for (a) $\mathrm{Re}_\tau = 86.15$ (b) $\mathrm{Re}_\tau = 121.84$

setting is the size of the simulation domain $L_x^+ \times L_z^+$ which is 4000×800 in the current study and in Xi and Graham [7] $L_x^+ = 360$ and $L_z^+ = 140 \sim 260$ depending on the Wi. As a result, the sequence and qualitative behaviours of different stages of DR are the same between the two domain sizes, but the quantitative magnitudes of the critical Wi and DR% for all transitions differ. In MFUs, the LDR-HDR transition occurs at Wi = 20 with DR% $\approx$ 15 and convergence to MDR is found at Wi = 27 and DR% $\approx$ 26; whereas in the extended domain, both these transitions are found at higher Wi and DR%. In a way, the restrictive domain of MFU compresses the transitions into a smaller parameter region but still preserves all qualitative aspects.

Figure 6 shows the mean velocity profiles of the $\mathrm{Re}_\tau = 86.15$ and $\mathrm{Re}_\tau = 121.84$ cases. The Newtonian profile at $\mathrm{Re}_\tau = 86.15$ is parallel to the PvK log law for $y^+ > 30$ but the intercept is slightly higher, because at this lowest Re the log-law layer is not fully developed. At $\mathrm{Re}_\tau = 121.84$, the Newtonian profile is already very close to the PvK log law and at $\mathrm{Re}_\tau = 172.31$ (not shown here) it completely overlaps the latter. Before the onset of DR, viscoelastic profiles are indistinguishable from the Newtonian ones and thus omitted from Figure 6. At LDR (Wi = 16 for both Re in Figure 6), the mean velocity profiles rise in the buffer layer region and remain parallel to the Newtonian case in the log-law region. At HDR (i.e. Wi = 32 for $\mathrm{Re}_\tau = 86.15$ and Wi = 48 for $\mathrm{Re}_\tau = 121.84$), the profiles lift up in the log-law layer showing slopes clearly higher than that
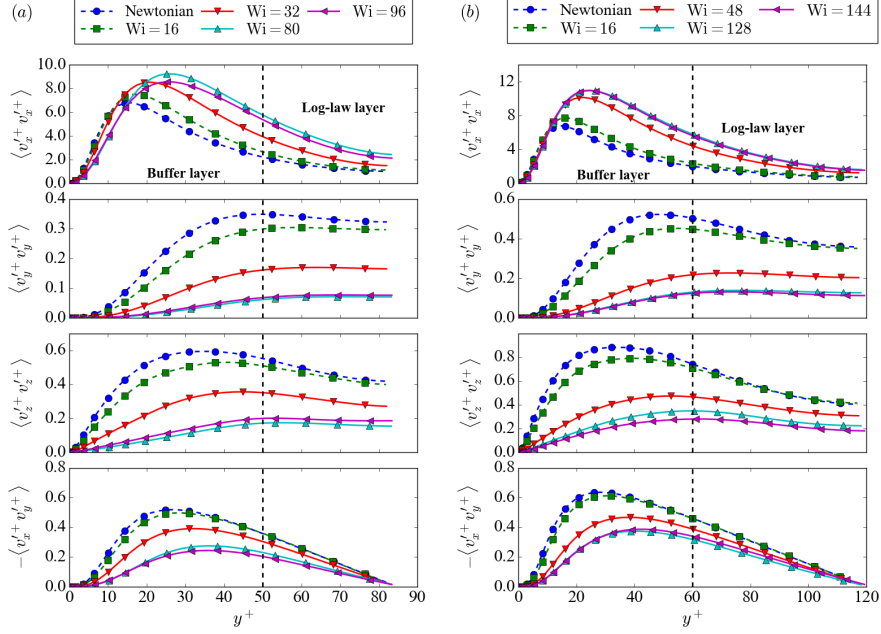
14

Figure 7: Reynolds stress profiles $(a)\mathrm{Re}_\tau = 86.15$ and $(b)\mathrm{Re}_\tau = 121.84$

of the PvK asymptote. For each Re_τ, two profiles are chosen in the MDR stage (i.e. $\mathrm{Wi} = 80$ and 96 for $\mathrm{Re}_\tau = 86.15$ and $\mathrm{Wi} = 128$ and 144 for $\mathrm{Re}_\tau = 121.84$)

280   to show the convergence of the mean velocity. At both Re_τ, the profiles are close to but still slightly below the Virk asymptote. Although it is a common practice in the literature to take the Virk log law as the criterion for identifying MDR, we note that it is only an empirical correlation for experimental data often gathered at higher Re than most computational studies. The appropriateness

285   of the Virk log law is even challenged recently [14]. As stated above, we take a literal interpretation and identify MDR as the asymptotic limit of DR with increasing Wi. The nature and definition of MDR are not the focus of this study.

Figure 7 shows the distribution of four components ($\langle v_x'^+ v_x'^+ \rangle$, $\langle v_y'^+ v_y'^+ \rangle$,

290    $\langle v_z'^+ v_z'^+ \rangle$ and $-\langle v_x'^+ v_y'^+ \rangle$) of the Reynolds stress across the channel at $\mathrm{Re}_\tau = 86.15$ and 121.84. For both Re and after onset, the streamwise Reynolds
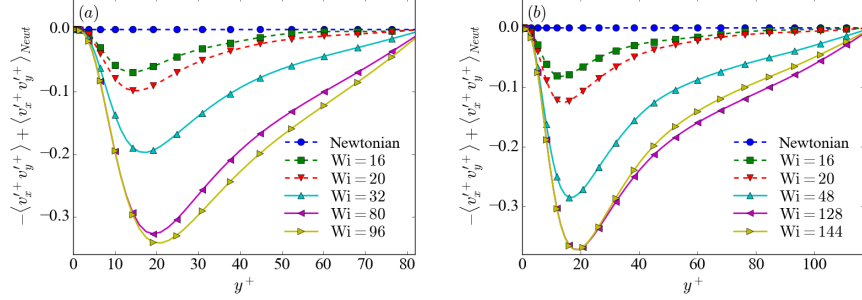
15

Figure 8: Deviation of the Reynolds shear stress from the Newtonian case: $(a)\mathrm{Re}_\tau = 86.15$ and $(b)\mathrm{Re}_\tau = 121.84$.

stress profiles rise up with increasing Wi while the wall-normal, spanwise, and shear components are all suppressed. All four components converge as MDR is reached. In addition to the commonly discussed change of shape in the mean velocity profile (Figure 6), the LDR-HDR transition can also be clearly iden-
²⁹⁵ tified with the changing Reynolds stress profiles as well especially of the xy shear component. From the bottom panels of Figure 7, it is clear that at LDR (Wi $= 16$ for both Re_τ), the suppression of the $-\langle v'^{+}_x v'^{+}_y \rangle$ profile is localized in the buffer layer $-5 \lesssim y^+ \lesssim 30$ and at higher y^+ the profile well overlaps with the
³⁰⁰ Newtonian one. By contrast, at higher Wi (after the LDR-HDR transition), the suppression extends across the whole channel. A vertical dashed line is drawn within the log-law layer as an eye guide to show the reduced magnitude there. This transition between local and global suppression is more clearly seen when the deviation of the Reynolds shear stress from the Newtonian case is plotted
³⁰⁵ in Figure 8.

Note that in our MDR cases, although $-\langle v'^{+}_x v'^{+}_y \rangle$ is significantly suppressed by polymers, its magnitude remains finite and differs from the Newtonian value by no more than one order of magnitude. Vanishing Reynolds shear stress is often cited in the literature as a key feature of MDR, an argument first made by
³¹⁰ Warholic et al. [10] based on their experimental observation. Later experimental and numerical observations were not always consistent with this conclusion and
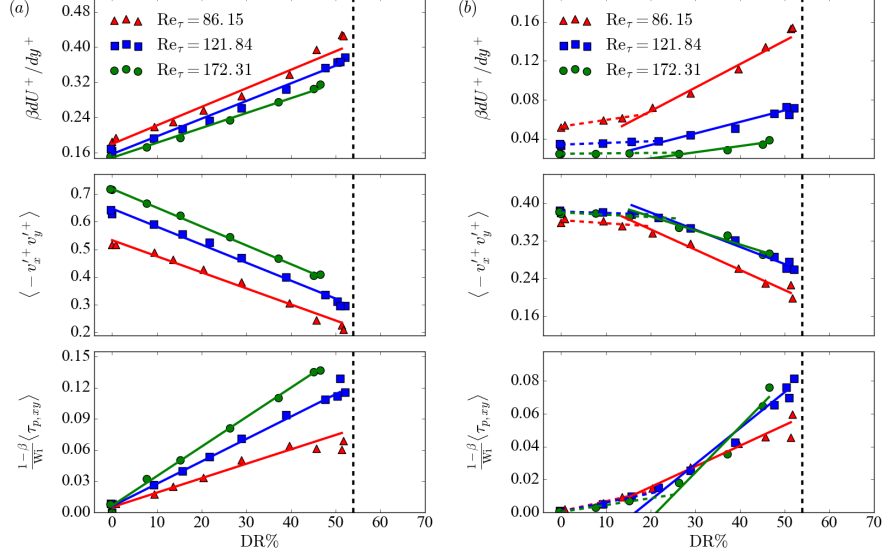
16

Figure 9: Correlation between different contributions to the total shear stress (Equation (11)) with varying DR% at $(a) y^+ = 25$ and (b) $y^+ = 0.6 \mathrm{Re}_\tau$. In panel (a), lines represent the linear regression results of all points; in panel (b), dashed lines are for the linear regression results of LDR and solid lines for HDR.

non-zero Reynolds shear stress is often seen even when the Virk MDR asymptote is reached [11, 12, 13]. Flow statistics at MDR is not our current focus and we do not intend to settle this debate in this paper. However, our observations do

315 indicate that for Reynolds shear stress it is the wall regions of suppression, not the magnitude itself, that determines the onset of HDR.

In other components, changes in the Reynolds stress magnitudes (increase in the streamwise component and decrease in other components) in the log-law layer all become augmented at the LDR-HDR transition. Notably, it even

320 results in a clear change of shape of the wall-normal profile: at LDR, same as the Newtonian limit, the profiles climb up to a maximum near $y^+ = 40$, followed by a steady decline at higher y^+, whereas at HDR, the profiles stay flat in the log-law layer.

Qualitative transitions observed in both Figures 6 and 7 indicate that funda-

17

mental changes have occurred in the turbulent dynamics of the log-law layer. To further tie these transitions to the phenomenological LDR-HDR transition, we compare the trends of quantity changes using multiple data points in both LDR and HDR regimes. Note that the Reynolds shear stress is related to the velocity gradient, which determines the log-law slope of the mean velocity profile, via

330 the shear stress balance

$$\left\langle \tau_{xy}^+ \right\rangle = \beta \frac{dU^+}{dy^+} + \left\langle -v_x'^+ v_y'^+ \right\rangle + \frac{1 - \beta}{\mathrm{Wi}} \left\langle \tau_{p,xy} \right\rangle. \tag{11}$$

The three components on the right-hand side of Equation (11) are the contributions of the mean viscous shear stress, Reynolds shear stress, and polymer shear stress to the total shear stress. Figure $9(a)$ and (b) show the quantitative correlation between these terms and DR% in the buffer layer (i.e. $y^+ = 25$) and

335 the log-law layer ($y^+ = 0.6\mathrm{Re}_\tau$), respectively.In the buffer layer (Figure $9(a)$), all three terms vary – increase for the viscous and polymer shear stresses and decrease for the Reynolds shear stress – nearly linearly with DR% between the DR onset and MDR. Comparing different Re, the viscous shear stress decreases and the Reynolds shear stress increases as Re increases, which is consistent with

340 previous observations in Newtonian flows [39, 40]. At higher Re (than those reported here), the Re-dependence of these shear stress terms is expected to be weaker according to the previous study of Housiadas and Beris [41]. Interestingly, for these two terms, the slope of the trendlines stays approximately the same with varying Re, suggesting that despite the significant weakening of tur-

345 bulence, polymer effects remain qualitatively similar in this layer. Meanwhile, the polymer term also shows a Re-dependence but the slope of the trendlines increases. On the other hand, in the log-law region(Figure $9(b)$), clear sharp transitions are found in all three terms between LDR and HDR. Before the LDR-HDR transition, variations in these quantities with increasing DR% are

350 barely existent, but in the HDR regime, a clear trend of either increase or decline is observed. Re-dependence is still observed but becomes less obvious as Re_τ grows higher, especially in the cases of Reynolds and polymer shear stresses. The turning point between these two behaviors puts the LDR-HDR transition at
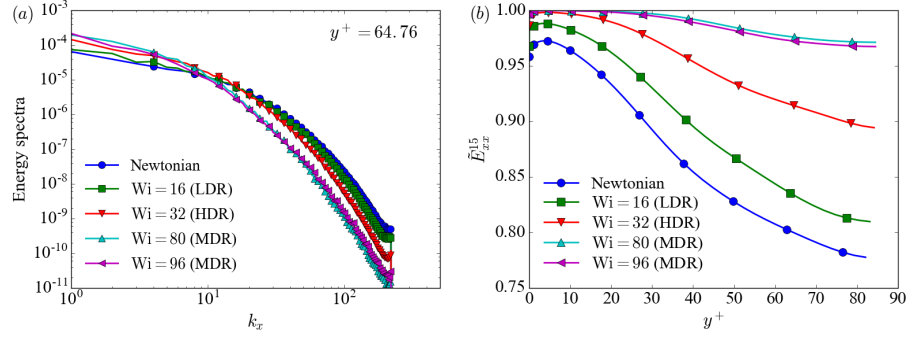
18

Figure 10: (a) The energy spectra (x-x component) of different Wi at $y^+ = 64$ and $Re_\tau = 86.15$ and (b) Proportion of energy contained in the large scales($k_x \leq 15$).

DR% ≈ 20, a value lower than the experimental transition point of DR% ≈ 35
³⁵⁵ reported by Warholic et al. [10].This is likely due to our lower Re: note that in
Figure 9(b) the transition point does shift toward higher DR% as Re_τ increases.
We stress here again that LDR-HDR is a qualitative transition in the turbulent
dynamics that is not tied to a particular quantitative magnitude of DR% for
different Re. Observations in Figure 9 are also consistent with our earlier hy-
³⁶⁰ pothesis that DR is a two stage process with different mechanisms: the first one
is triggered at the DR onset and takes effect in the buffer layer and the second
one gives rise to HDR in which the log-law layer dynamics becomes affected.

To further inspect the changing flow statistics in the log-law layer, the energy
spectrum of the streamwise velocity E_{xx} (defined in Equation (7)) is calculated
³⁶⁵ in the log-law layer and plotted in Figure 10(a). As Wi increases, the profile
is raised at smaller k_x and reduced at larger ones. This is consistent with
the observation in previous studies that polymer additives suppress small scale
fluctuations and strengthen energy-containing large-scale structures [10, 42, 43].
The effect becomes apparently amplified in HDR, which is more clearly observed
³⁷⁰ when we calculate the proportion of energy contained in the 15 leading modes

$$\tilde{E}_{xx}^{15} = \sum_{k=0}^{15} E_{xx}^{(k)} / \sum_{k=0}^{\infty} E_{xx}^{(k)} \tag{12}$$

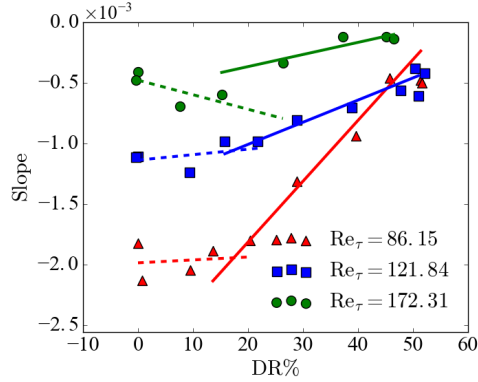and plot it as a function of y^+ in Figure 10. As Wi increases, the accumulated

19

Figure 11: Characteristic slope of the accumulated energy profile (Figure 10(b)) in the bulk region of the channel ($|y| \leq 0.5$). The solid and dash lines are obtained with linear regression of the data in the HDR and LDR stages, respectively.

energy contained in the large scales increases, consistent with the increasing importance of the large-scale turbulent structures. In all cases, the profiles decrease as they approach the center of the channel. For Newtonian and LDR
375 cases, the decline is rather steep: the latter is nearly parallel to the former for the whole channel. Therefore, LDR preserves the same near-wall turbulent dynamics typical of Newtonian flow, where the buffer layer is dominated by recurrent coherent vortical motions and their outward eruptions, the so-called "bursting" events, generate intense small-scale fluctuations at larger y^+ [44].
380 DR is caused by an across-the-board suppression of turbulent motions extending over the entire channel. By contrast, for the HDR cases, profiles are gradually lifting up in the log-law layer and near the center. This suggests that at the HDR and MDR stages, polymers become more effective in suppressing the small-scale fluctuations at high y^+, which supports our hypothesis that a second mechanism
385 is triggered at HDR for DR in the log-law layer. This change of profile shape can be shown to correspond exactly to the LDR-HDR transition when we take the part of each profile in Figure 10 within the bulk of the channel – defined here as $|y| \leq 0.5$, calculate a profile slope using linear regression, and plot this characteristic slope in Figure 11 versus DR%. It is clear that at LDR, the
390 characteristic slope is nearly flat with increasing DR% and the slope starts to
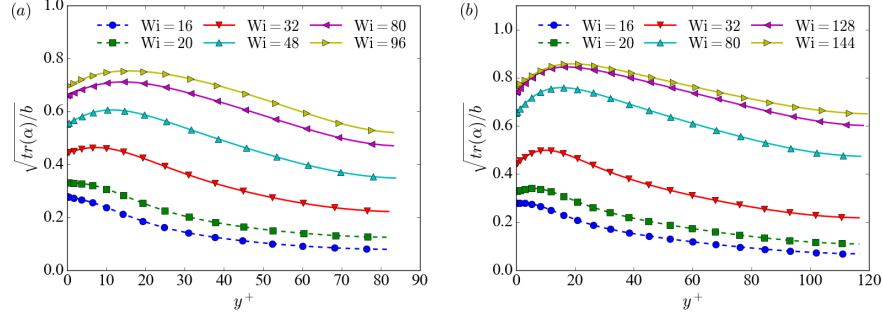
20

Figure 12: Normalized profiles of the square root of the trace of the polymer conformation tensor: $(a)\text{Re}_\tau = 86.15$ and $(b)\text{Re}_\tau = 121.84$

increase only in HDR. With increasing Re, the characteristic slope increases (becomes less negative) at the Newtonian and LDR end: i.e., the profiles of $\tilde{E}_{xx}^{15}$ are flatter near the channel center. This is however a trivial observation. It is important to be reminded that the characteristic slope is defined in terms 395 of the wall-normal position in the outer unit – i.e., $|y| \leq 0.5$ – and it does not correspond to the same wall layer in the inner unit. At higher Re, the slope reflects more of the turbulent core than the boundary layer. Likewise, the universal cutoff of $k_x \leq 15$ used in the definition of $\tilde{E}_{xx}^{15}$ is also arbitrary and affects results from different Re differently. Comparison of the slope in Figure 11 400 is only meaningful at the same Re and any interpretation of the Re-dependence can be misleading.

As for the polymer conformation statistics, we show the normalized profiles of the square root of the trace of the polymer conformation tensor α at $\text{Re}_\tau = 86.15$ and 121.84 in Figure 12. This quantity is essentially proportional to 405 the average end-to-end distance of the polymer chains. As expected, polymer extension increases with Wi, but interestingly the trend does not stop in the MDR stage: i.e., even after the flow statistics have converged, polymer extension continues to increase. There is also a clear qualitative difference between low and high Wi, which occurs roughly at the LDR-HDR transition. At lower Wi, 410 polymer extension is highest at the wall, where the mean shear rate is highest,

21

(*a*) Newtonian

(*b*) Wi = 16 (LDR)
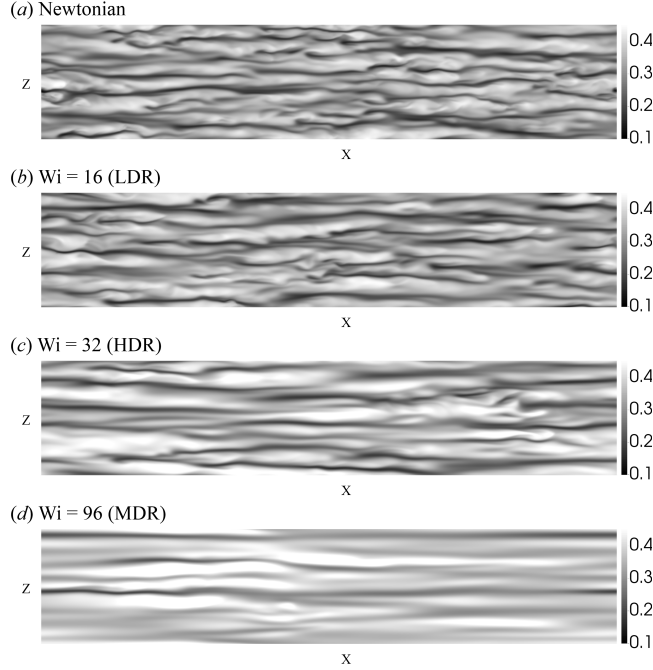
(*c*) Wi = 32 (HDR)

(*d*) Wi = 96 (MDR)

Figure 13: Instantaneous streamwise velocity in the xz plane at $y^+ = 20$.

and it declines monotonically with y^+. At higher Wi, a maximum is found in the buffer layer between $y^+ = 10$ and 20. A similar change of peak position was also observed in MFUs [7] and it indicates a qualitative shift in the polymer-turbulence interaction.

3.2. Turbulence structures

To unravel the turbulent dynamics behind these changing flow statistics, we first turn to the flow patterns and vortex structures. We will start with velocity distributions which have been widely discussed in the literature. We will then show that the changing velocity patterns are a reflection of a change in the vortex distribution and topology.

3.2.1. Turbulence localization: visualization and quadrat analysis

Figure 13 shows the streamwise velocity distribution at $y^+ = 20$ for Newtonian, LDR, HDR and MDR stages at $\mathrm{Re}_\tau = 86.15$. The alternating bright

22

and dark stripes correspond to the high- and low-speed streaks, typical of near-wall coherent structures. It is clear that as Wi increases, the length of velocity streaks increases while the curvature of the streaks decreases. For Newtonian and LDR cases, the streaks wiggle around as they extend downstream, whereas in HDR and MDR, the streaks are wide and straight in shape and wrinkles become spotty. These changes are reported in various prior experimental and numerical studies [13, 43, 45, 46].

Vortices in the flow field are identified by the Q criterion [47, 48], where

$$Q \equiv \frac{1}{2} \left(\|\mathbf{\Omega}\|^2 - \|\mathbf{\Gamma}\|^2 \right) \tag{13}$$

is the difference between the Frobenius norms of the vorticity tensor

$$\mathbf{\Omega} \equiv \frac{1}{2} \left(\boldsymbol{\nabla} \boldsymbol{v} - \boldsymbol{\nabla} \boldsymbol{v}^T \right) \tag{14}$$

and the rate of strain tensor

$$\mathbf{\Gamma} \equiv \frac{1}{2} \left(\boldsymbol{\nabla} \boldsymbol{v} + \boldsymbol{\nabla} \boldsymbol{v}^T \right). \tag{15}$$

A pure shear flow has $Q = 0$ and in turbulent flow large positive and negative Q values correspond to regions dominated by rotational and extensional flows, respectively.

Isosurfaces of $Q = 0.7 Q_{\mathrm{rms}}$, where Q_{rms} is the root-mean-square of the Q field in that domain, are shown in Figure 14 for the same four instants of Figure 13. As Wi increases, not only is the vortex strength weakened – which can be judged from the isosurface level ($\propto Q_{\mathrm{rms}}$) and is expected because polymers are known to suppress turbulence, but the distribution pattern also seems to have changed. In the Newtonian and LDR (Wi = 16) cases, the domain is densely populated by a large number of vortices and the distribution is mostly uniform in space. From the upstream side (left side), the vortices originate from the wall (light color) and lift upwards (darker color) as they extend downstream. Most of them do not exceed ≈ 300 wall units and despite the low Re, the so-called "hairpin" vortices are already observed. A symmetric hairpin is developed when two streamwise vortices lift up at the downstream end and connect via
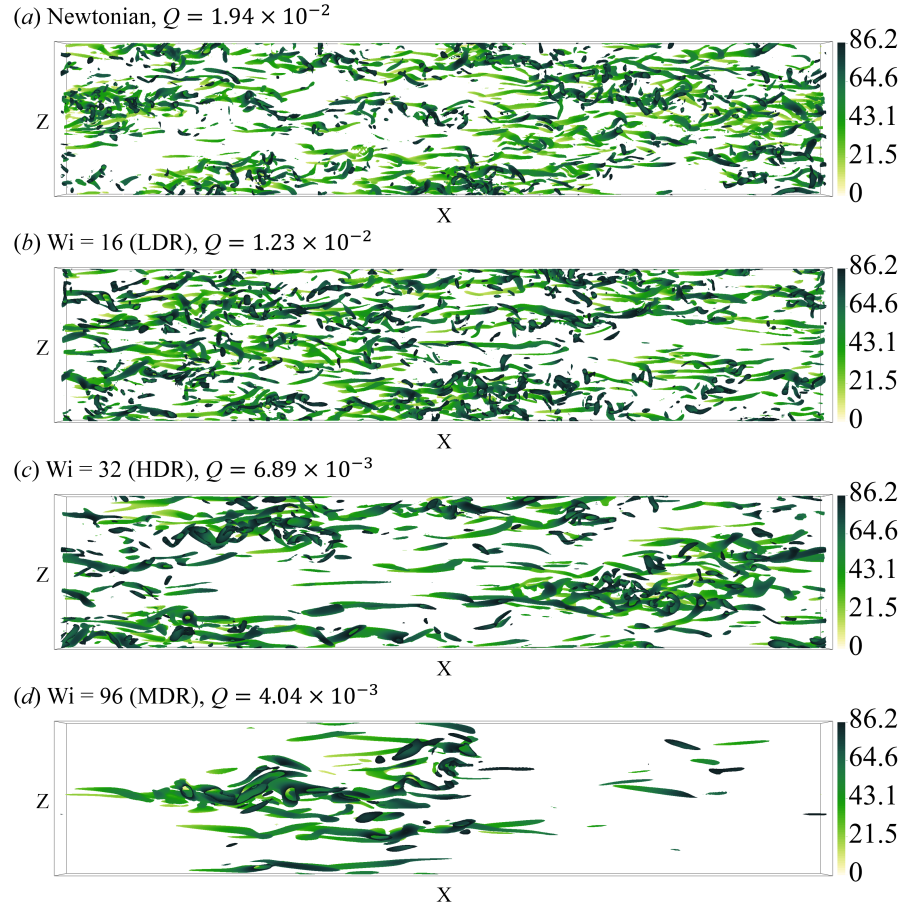
(*a*) Newtonian, $Q = 1.94 \times 10^{-2}$

(*b*) Wi = 16 (LDR), $Q = 1.23 \times 10^{-2}$

(*c*) Wi = 32 (HDR), $Q = 6.89 \times 10^{-3}$

(*d*) Wi = 96 (MDR), $Q = 4.04 \times 10^{-3}$

Figure 14: Typical snapshots of the vortex structures at $\mathrm{Re}_\tau = 86.15$ (top view; only vortices in the bottom half of the channel are shown). Isosurfaces of $Q = 0.7Q_{\mathrm{rms}}$ are chosen to represent the vortex surfaces. The color shade (from light to dark) maps to the wall distance y^+ (from 0 to Re_τ).
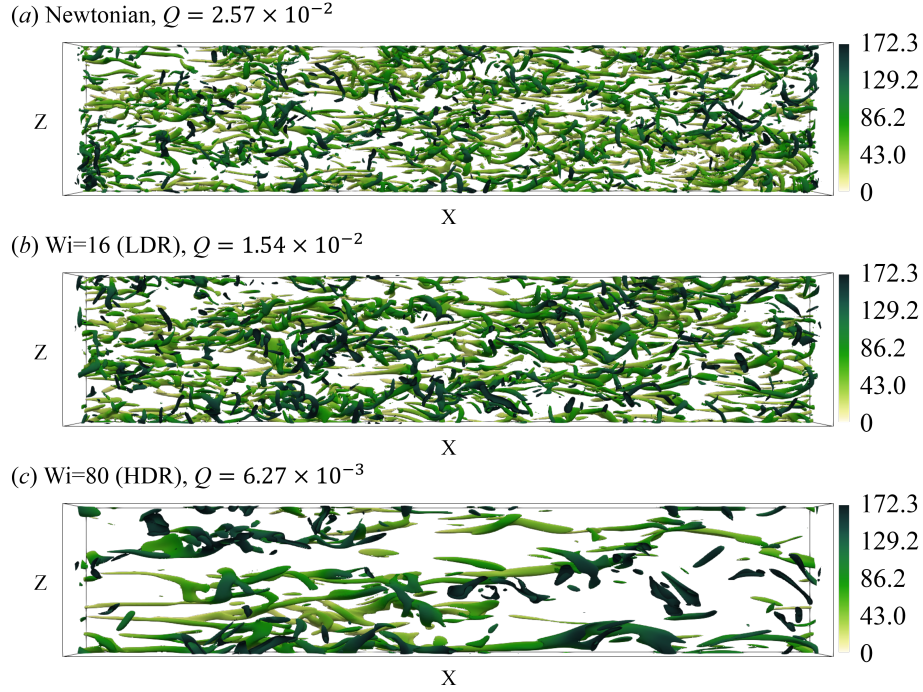
24

(*a*) Newtonian, $Q = 2.57 \times 10^{-2}$


```
172.3
129.2
86.2
43.0
0
```

(*b*) Wi=16 (LDR), $Q = 1.54 \times 10^{-2}$


```
172.3
129.2
86.2
43.0
0
```

(*c*) Wi=80 (HDR), $Q = 6.27 \times 10^{-3}$


```
172.3
129.2
86.2
43.0
0
```

Figure 15: Typical snapshots of the vortex structures at $\mathrm{Re}_\tau = 172.31$ (top view; only vortices in the bottom half of the channel are shown). Isosurfaces of $Q = 0.7 Q_{\mathrm{rms}}$ are chosen to represent the vortex surfaces. The color shade (from light to dark) maps to the wall distance y^+ (from 0 to Re_τ).

an "arc" in the spanwise direction. More often the hairpin is incomplete or asymmetric where one of the legs is not clearly developed. By contrast, in the case of HDR (Wi = 32) and MDR (Wi = 96), the distribution becomes clearly heterogeneous where vortices tend to agglomerate: i.e., turbulence is more localized and regions between those vortex clusters are nearly laminar. Vortices also become elongated and most remain aligned in streamwise direction. Indeed, the smooth streak patterns observed in Figure 13 for HDR (and MDR) are simply a reflection of the turbulence localization, where the straightened streaks correspond to the quasi-laminar regions and the spotty wrinkles result from localized vortex clusters.

Vortex structures at $\mathrm{Re}_\tau = 172.31$ are also identified by isosurfaces of $Q =$

25

$0.7Q_{\mathrm{rms}}$ and shown in Figure 15. Same as the lower Re case, distinct aggregation of vortices also occurs at the HDR stage (Wi = 80). Compared with the low Re case, the major difference is the presence of a considerable number of hairpin vortices in Newtonian flow, which is commonly observed in the literature at similar Re levels [49, 50]. These hairpin-like vortices are mostly asymmetric with one leg extending much longer than the other. Qualitative changes in the flow structures and patterns between LDR and HDR have been noticed in the literature at even higher Re (e.g., $\mathrm{Re}_\tau = 395$ in Li et al. [13]). Vortex clustering and localization reported here offer an effective explanation for those observations. For example, the emergence of larger quiescent regions results in areas with straight and elongated streaks in velocity contour plots and the localized vortical structure corresponds to isolated wrinkles on those streaks (see fig. 13 here as well as, e.g., fig. 4 of Li et al. [13] and fig. 17 of Housiadas et al. [43]).

In order to quantitatively analyze the level of turbulence localization at high-Wi turbulence, we adopt the so-called quadrat analysis [51]. In this algorithm, the computational domain is divided into an array of rectilinear cells in the xz plane. Within each cell,

$$p \equiv V_{\mathrm{turb}}/V_{\mathrm{cell}} \tag{16}$$

is the fraction of the volume occupied by turbulence V_{turb} over the total cell volume V_{cell}. Here, turbulent regions are identified as those where $Q > 0.7Q_{\mathrm{rms}}$. The extent of localization is quantified by the coefficient of variation

$$\mathrm{CV} = \frac{s_p}{\bar{p}} \tag{17}$$

where s_p and $\bar{p}$ are the standard deviation and the mean of the p values of individual cells. Obviously, when turbulent distribution is more heterogeneous, there will be a larger disparity between the p values of different cells, leading to a larger ratio of its standard deviation to the mean.

Results of this quadrat analysis are presented in Figure 16. Since the choice of cell size is arbitrary, we tested multiple sizes to make sure that our conclusions
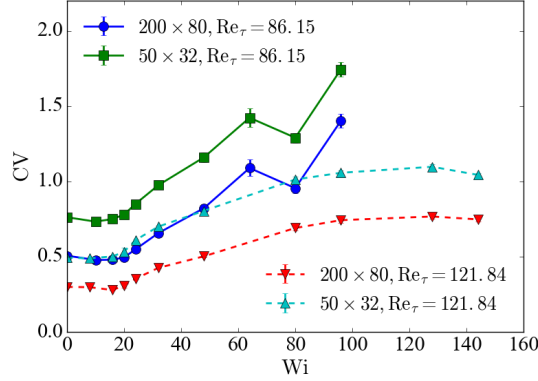
Figure 16: The three dimensional quadrat analysis at $\mathrm{Re}_\tau = 86.15$ and $\mathrm{Re}_\tau = 121.84$. Two cell sizes are reported: $l_x^+ \times l_y^+ = 200 \times 80$ and 50×32.

do not depend on this artificial parameter; two of the sizes are tested, i.e., $l_x^+ \times l_z^+ = 200 \times 80$ and 50×32, are shown in this figure. It is clear that the cell size only affects the quantitative magnitude of CV without changing the qualitative trend of the profiles. At lower Wi (still above the DR onset), CV remains at the same level as the Newtonian case. After the LDR-HDR transition ($\mathrm{Wi}_{\mathrm{LDR\text{-}HDR}} = 24$), this number steadily increases: i.e., turbulence becomes more localized.

Similar as the case in Figure 11, differences in CV between the two Re do not lead to any physically meaningful conclusion. Both the cell size and the cutoff threshold of Q are arbitrarily chosen parameters with unknown Re-dependence: comparison is only meaningful at the same Re. We have also tested a two-dimensional variant of the quadrat analysis, where the xz-planar average Q values – at the $y^+ = 25$ (buffer layer) and $y^+ = 0.6\mathrm{Re}_\tau$ (log-law layer) planes – are used in place of Q_{cell} in the identification of turbulent regions. The results are similar to those of the three-dimensional version shown in Figure 16 (and thus not shown here), which indicates that the clustering of vortices and turbulence localization are occurring across the domain as the flow enters HDR.
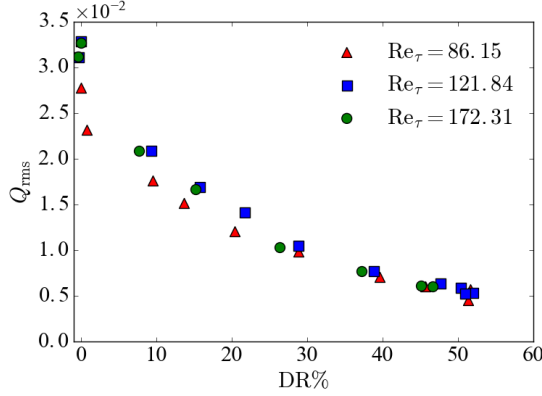
27

Figure 17: The root-mean-square of Q with varying DR%

3.2.2. Discussion: relationship with flow statistics

[505] The above observations are consistent with our initial hypothesis that DR is a two stage process. At the onset of DR, polymers undergo the coil-stretch transition and start to suppress all vortical motions. This across-the-board vortex suppression occurs throughout all stages of DR after the onset. As shown in Figure 17, the magnitude of Q steadily decreases with increasing DR% in both [510] LDR and HDR stages. The localization of turbulence, however, only occurs in HDR, which could be the second mechanism for DR and responsible for the qualitatively changes in flow statistics.

The observation of turbulence localization at the transition to HDR resonates with the spatio-temporal intermittency between active and hibernating [515] turbulence discussed earlier [22, 26, 27]. These two concepts are clearly related but the distinction between them should not be overlooked. Of course, the localization and clustering of turbulent vortices open up large regions in the domain with little turbulent activity. This is consistent with the higher fraction of hibernating turbulence at high Wi reported in Xi and Graham [27]. On the [520] other hand, in theory one may as well increase the hibernation fraction without relying on turbulence localization: i.e., by enlarging the hibernating spots evenly across the domain. Indeed, turbulence localization requires the cooperation of coherent structures (shown in Section 3.2.3) over longer length scales
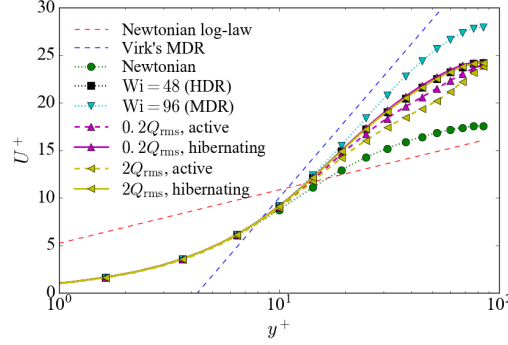
28

Figure 18: Conditional average mean velocity profiles of active and hibernating regions at $\mathrm{Re}_\tau = 86.15$ and $\mathrm{Wi} = 48$. Results from two different cutoff magnitudes Q_{cutoff} are shown in comparison with the time-average Newtonian and $\mathrm{Wi} = 48$ profiles.

not captured in MFUs (from which the active-hibernating framework was first proposed). The nature of this cooperation is the focus of Section 3.3, which is also central to the understanding of HDR.

On the surface, associating HDR with a higher fraction of hibernating regions offers a straightforward explanation for the different flow statistics at HDR. To see this, we need to first make two hypotheses: (1) after the DR onset, polymers suppress buffer-layer structures in active turbulence, which causes DR there but leaves the log-law layer flow statistics largely unaffected and (2) after the LDR-HDR transition, hibernating turbulence becomes statistically significant. Since the mean velocity profile in hibernating turbulence is known to have a much higher slope, not only in the buffer layer but across the channel, its higher fraction will naturally lead to higher log-law layer slope in the time-average profile. To test this, we first divide the domain along the xz plane according to the comparison between the local y-averaged $|Q|$ magnitude

$$\overline{|Q|}_y = \frac{1}{\mathrm{Re}_\tau} \int_0^{\mathrm{Re}_\tau} |Q| dy^+ \tag{18}$$

and a cutoff value Q_{cutoff}: regions with $\overline{|Q|}_y > Q_{\mathrm{cutoff}}$ are considered active and those with $\overline{|Q|}_y \leq Q_{\mathrm{cutoff}}$ hibernating.Conditional average mean velocity profiles

29

of these two groups, using two drastically different values of $Q_{\text{cutoff}} = 0.2Q_{\text{rms}}$ and $2Q_{\text{rms}}$, are shown in Figure 18. Contrary to the first hypothesis above, even for active regions, the mean velocity profile in the log-law layer has clearly risen up, showing much higher slopes than the PvK log law. This result indicates that the binary division into active and hibernating regions while neglecting any correlations between them is too simplified to explain the phenomenology of HDR.

3.2.3. Percolation Analysis

A simple extension of the active-hibernating framework from MFU to an extended domain would imply that there is no difference in vortex topology within the active regions between LDR and HDR: at high Wi, polymers only quench the turbulent activity in parts of the domain (hibernating regions) while vortex dynamics in the rest (active regions) are generated from the same instability as in Newtonian turbulence [7, 27]. Here, however, using the percolation analysis proposed by Lozano-Durán et al. [52], we discover a fundamental shift in the vortex topology that accompanies the localization of turbulence.

Recall the Q-criterion used in Figure 14, the choice of the threshold value of Q for vortex identification is largely arbitrary. The resulting vortex configuration clearly depends on this choice: as $Q_{\text{threshold}}$ increases, fewer and fewer regions satisfy the criterion, resulting in fewer and smaller vortices being identified. Vortex configuration with the increasing threshold magnitude, measured by the non-dimensional H parameter defined with

$$Q_{\text{threshold}} \equiv HQ_{\text{rms}}, \tag{19}$$

is shown in Figure 19. For each H, interconnected vortices are considered to form a vortex cluster and coded with the same color in Figure 19. (Vortices are determined to be connected when at least two grid points, one from each isosurface, are immediately adjacent to each other.) Identified clusters are then ranked according to their volumes and only larger clusters that accumulatively account for 80% of the total vortex volume in the domain are shown (for the
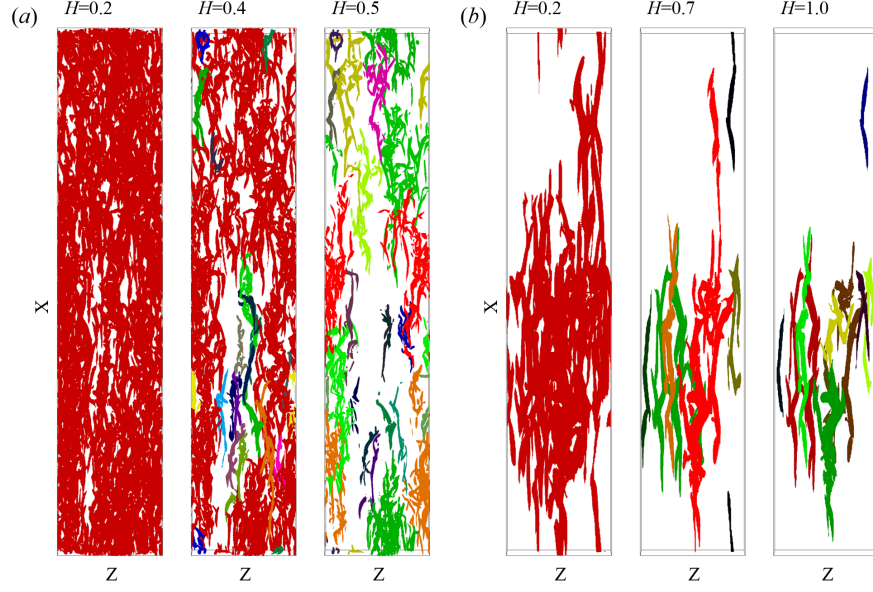
30

Figure 19: Vortex decomposition with increasing H (normalized threshold Q value for vortex identification; see Equation (19)) in the percolation analysis: (a) Newtonian, $\mathrm{Re}_\tau = 86.15$ and (b) Wi = 96, $\mathrm{Re}_\tau = 86.15$. Each interconnected vortex cluster is coded with the same color.
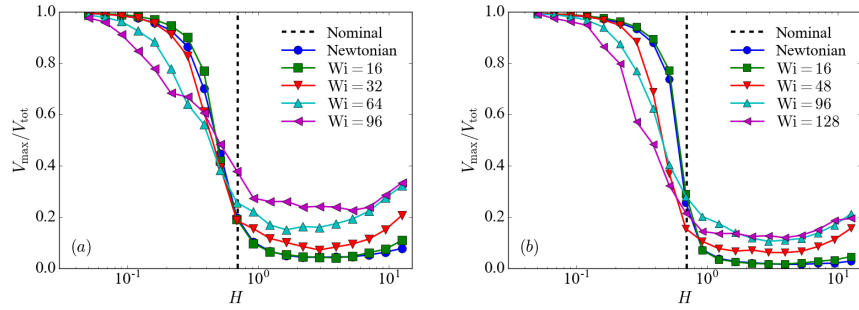

Figure 20: Percolation diagrams: (a)$\mathrm{Re}_\tau = 86.15$ (b)$\mathrm{Re}_\tau = 121.84$. Vertical dashed lines mark the $Q_{\mathrm{threshold}} = 0.7 Q_{\mathrm{rms}}$ used in Figure 14.

$H = 0.5$ image of the Newtonian case the cutoff is 60%). This is to eliminate the large number of small vortex fragments to clear the view.

In Newtonian turbulence (Figure 19(a)), at $H = 0.2$, the threshold is lower than even the Q magnitude of the weak rotational motion between vortex cores. These regions form "tunnels" that connect the main vortex bodies, resulting in an interconnected network that percolates the domain. As H increases to 0.4 and 0.5, the "tunnels" quickly break and the percolating network decomposes into separate vortex clusters, marked by different colors. This process is quantified by the ratio of the volume of the largest vortex cluster $V_{\max}$ to the total volume of all vortices identified V_{tot} and plotted in Figure 20. As shown in Figure 19(a), at the lowest H all vortices belong to the same cluster and therefore $V_{\max}/V_{\mathrm{tot}} = 1$. For the Newtonian case, raising H to around 0.5 triggers a quick collapse of the percolating network into much smaller clusters. Accordingly, $V_{\max}/V_{\mathrm{tot}}$ drops sharply since now even the largest cluster is only a small fraction of the total volume. The ratio stays almost constant as H increases beyond 1, indicating that individual clusters shrink in size proportionally while keeping the volume ratio between themselves. Lozano-Durán et al. [52] suggested that the proper threshold for vortex identification should fall within the transition between percolating and non-percolating behaviors. Our choice of $H = 0.7$ used in Figure 14 is within this range.

The $V_{\max}/V_{\mathrm{tot}}$ curve for LDR is nearly identical to the Newtonian case. At HDR, the transition period still centers around $H \sim 0.5$ but the decline of $V_{\max}/V_{\mathrm{tot}}$ is smoother and the transition extends over a larger range of H. At the highest Wi shown in Figure 20 – i.e., 96, the transition starts at H well below 0.1. This indicates that the percolation disintegration evolves into a continuous process. The corresponding vortex configuration is shown in Figure 19(b). At H as low as 0.2, a clear vortex cluster dominates the domain and no vortical structures are found in the laminar-like (hibernating) regions, reaffirming the true localization of turbulence. As H increases, no sudden disintegration is observed, indicating that the vortices in the cluster are closely connected with strong mutual interaction. The $V_{\max}/V_{\mathrm{tot}}$ ratio only decreases smoothly because

the tips of the "tentacles"of the cluster are gradually etched away with higher

600 H. Disintegration of the cluster is not observed until H is close to $O(1)$ and even there the process is progressive with new vortices being shed off with each increment of H. The large H magnitude required to break the cluster and the stepwise nature of its disintegration show that the interaction between vortices in the same cluster is stronger than the "tunnels" between clusters

605 observed in the Newtonian case. All in all, the percolation analysis reveals that the vortex dynamics at HDR becomes qualitatively changed where vortices are generated and sustained in large clusters with strong mutual interactions, whereas at LDR the process appears more stochastic. This difference leads to the apparent turbulence localization.

610 *3.3. Proposed mechanism*

We have so far demonstrated that the LDR-HDR transition is not simply a quantitative effect of the level of DR, but a qualitative transition likely involving two different stages of DR mechanisms. The transition is associated with a range of qualitative changes in flow statistics, behind which turbulent activities

615 are found to become localized. Although the first mechanism of DR, which sets its onset, is well understood as a generic across-the-board weakening and suppression of turbulent fluctuations [13, 19], the nature of the second mechanism, which drives the LDR-HDR transition, is unknown. Here, we make the first attempt at its mechanistic understanding by proposing a possible mechanism

620 that is compatible with currently known observations.

We start our discussion by revisiting the self-sustaining dynamics of Newtonian turbulence. Schoppa and Hussain [53] summarized the vortex regeneration mechanisms proposed in the literature into two major categories (Figure 21). The first is what we will refer to as the "streak-instability mechanism". Upward

625 ejection of near-wall fluid by streamwise vortices forms low-speed streaks. A strictly x-independent streak is stable but as the streak intensifies (i.e., larger contrast between low- and high-speed streaks), it becomes increasingly susceptible to x-dependent perturbations, which leads to the so-called streak breakdown
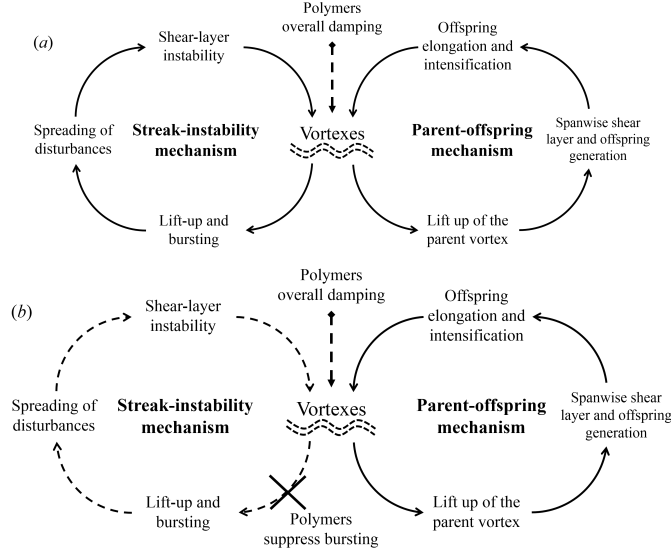
33

Figure 21: Vortex regeneration mechanism and polymer effects thereon in (*a*) LDR and (*b*) HDR

and the generation of streamwise vortices. This process is not only important for understanding the self-sustaining process of near-wall turbulence [54], streak breakdown is also a central step in the laminar-turbulent transition [55, 56]. In the second so-called "parent-offspring mechanism", a "parent" vortex lifts up at its head and instability of the shear layer between the vortex and the wall gives rise to a new "offspring" vortex. In this scenario, the new vortex is generated immediately next to its parent, implying strong correlation and spatial proximity between them. On the other hand, although the streak-instability mechanism does not require any immediate parent vortex, existing vortices still influence the generation of new ones. For example, the bursting of existing vortices generates perturbations that can destabilize streaks elsewhere in the domain. Obviously, this link between existing and new vortices is indirect and not necessarily local, compared with the parent-offspring mechanism. Finally, we note that this binary categorization is simplistic and there are a number of different mechanisms within either category. But it suffices for our discussion
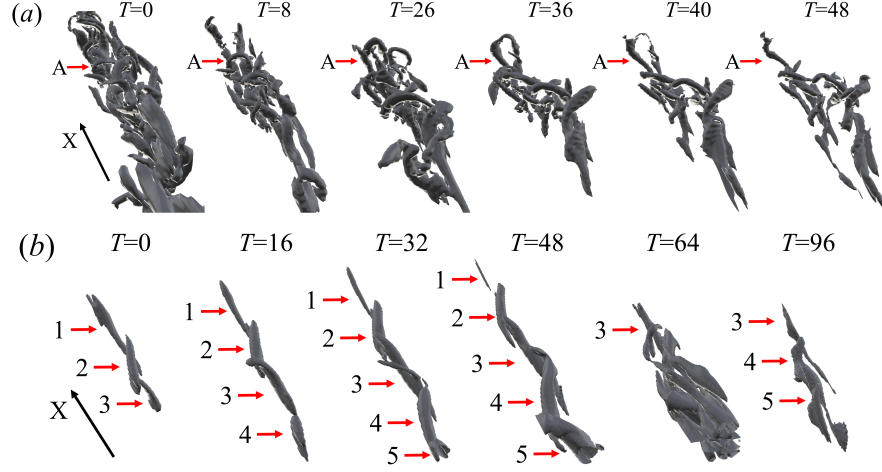
34

Figure 22: Typical vortex evolution scenarios observed in our DNS at $\mathrm{Re}_\tau = 86.15$: (a) streak-instability mechanism (Newtonian) and (b) parent offspring mechanism (Wi = 96).

on the vortex dynamics leading up to HDR.

Both mechanisms are observed in our DNS. In Figure 22, we pick and show one typical scenario for each case. Figure 22(a) shows a typical life cycle of a hairpin vortex following the streak-instability mechanism, which is found in Newtonian turbulence. At $T = 0$, a small tentacle-like vortex lifts up from a packet of streamwise vortices and connects with a neighbouring one at $T = 8$ to form a hairpin vortex (Vortex A). As this vortex pair evolves from an initial parallel configuration to a three-dimensional hairpin, the low-speed streak sandwiched between them (not shown) twists with the instability. The hairpin grows from a C-shaped arch ($T = 8$) to a Ω-shaped structure with its head lifting up towards the bulk of the flow ($T = 36$). At $T = 40$, the arch bursts and disappears from the view, with only one leg left behind at $T = 48$. Although difficult to show here in an extended turbulent domain, in our recent study [57] where the vortex growth and bursting process were tracked in an MFU, it was observed that the bursting of coherent vortices generates strong small-scale fluctuations that quickly propagate across the MFU. Borrowing that knowledge, we may postulate that the bursting event at $T = 40$ gives rise to small-scale fluctu-

35

ations that can spread and trigger instabilities in other streaks, thus completing the vortex regeneration cycle.

The self-sustaining process of Newtonian turbulence includes both streak-instability and parent-offspring mechanisms. These two processes offer two parallel pathways whereby the vortex dynamics can be continuously regenerated. Our simulations show that the situation changes at high Wi where the streak-instability process is rare and the parent-offspring pathway becomes exposed. A typical scenario is shown in Figure 22(b). Compared with the Newtonian case, much fewer hairpin vortices are observed at high Wi, which was also reported by Yarin [58] and was further supported by Kim et al. [59] through their dynamical simulations of counter-rotating pairs of quasistreamwise vortices. These streamwise vortices often align head-to-tail to form a string ($T = 0$), which was also observed by Li et al. [13], Kim et al. [60] at higher Re. In the vortex string, new vortices are often generated at the upstream end of their parents (e.g., the births of vortices 4 and 5 at $T = 16$ and 32), effectively extending the string against the oncoming flow. Interestingly, this order of vortex generation – i.e., from downstream to upstream, is opposite to the typical observation reported in Newtonian turbulence, where the offspring is more likely to be generated at the downstream side of the parent [61], although the reversed order was also occasionally observed in the Newtonian case [62]. In addition to suppressing the formation of hairpins, vortex lift-up or eruption and its subsequent bursting is also prevented. Overall, streamwise vortices are stabilized by the high polymer elasticity, allowing them to extend to much longer length scales (see Figures 13 and 14 and also refer to [59, 63, 64]). Not able to burst, the vortices eventually decay and disappear (vortices 1 & 2 at $T = 64$). This again is consistent with observations made in Bai and Xi [57] that polymers are able to help the flow bypass the bursting of vortices and avoid small-scale fluctuations. Here, instead of bursting, we only observed a mild and temporary swelling and proliferation of vortices at $T = 64$. This regeneration dynamics, that vortices are more often generated as an offspring of a nearby parent, explains perfectly why vortical structures are more localized at high Wi and why vortices within
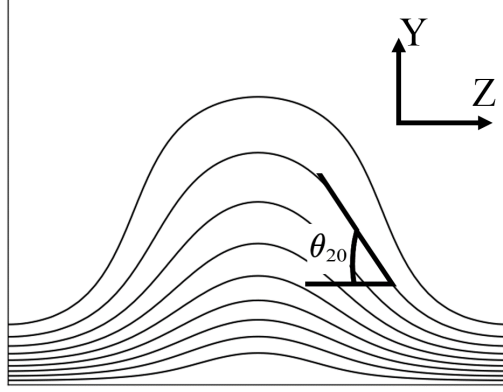
36

Figure 23: Schematic of the definition of the streak lift angle measured at $y^+ = 20$: θ_{20}. Solid lines represent the contour of streamwise velocity.

the same clusters are strongly correlated (see Figure 19). In addition, the suppression of hairpins and their lift-up and eruption at larger y^+ can also explain the suppressed Reynolds shear stress in the log-law layer. And since bursting is bypassed, intense small-scale fluctuations are avoided, which is consistent with the larger proportion of energy accumulating in large scale structures in the log-law layer (Figure 10).

After the direct comparison between the vortex regeneration dynamics of a Newtonian and high-Wi cases, we now need to show that the suppression of the streak-instability pathway does indeed correlate with the LDR-HDR transition. According to [53], the relative stability of a streak is determined by its "strength", which basically describes by how much the base flow has been distorted by the upward ejection of the low-speed streak, which creates spanwise variation or contrast in v_x. As sketched in Figure 23, the strength is quantified locally by the streak lift angle

$$\theta \equiv \arctan\left(\frac{|\omega_y|}{|\omega_z|}\right) \qquad (20)$$

where ω_y and ω_z are the wall-normal and spanwise components of the local vorticity. The stability of low-speed streaks is measured by their characteristic

37

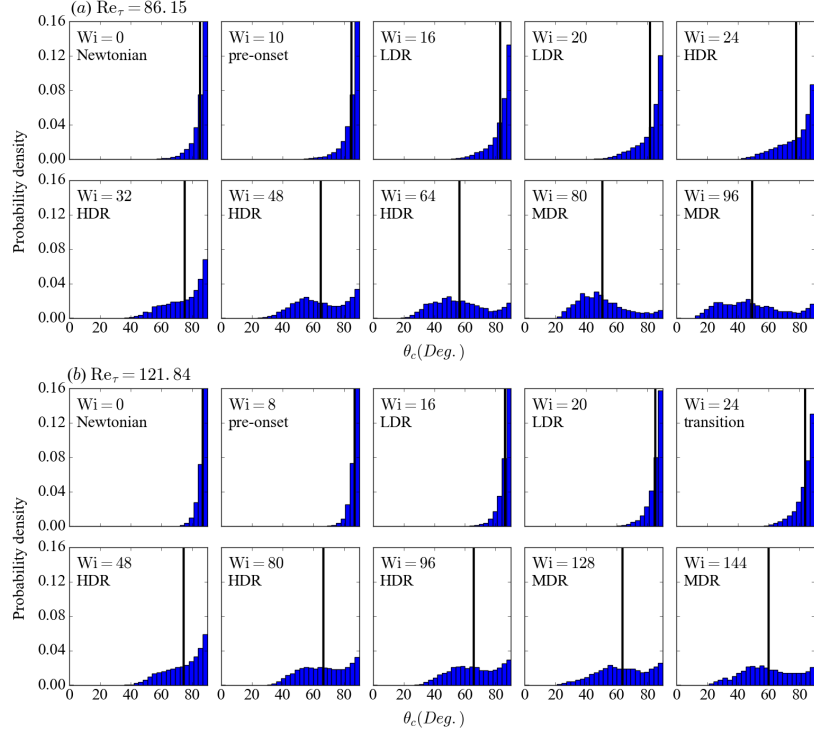Figure 24: Probability density functions of the characteristic streak lift angle at (*a*) $\mathrm{Re}_\tau = 86.15$ and (*b*) $\mathrm{Re}_\tau = 121.84$. Vertical lines mark the mean value of each distribution.

lift angle

$$\theta_c \equiv \max\left(\theta_{20}\right) \tag{21}$$

at the $y^+ = 20$ plane. Here, regions with $v'_x \leq 0$ are first identified as the low-speed streak regions; local maxima along the x direction that fall into these regions are collected into the sample pool of θ_c.

Figure 24 shows the probability density functions (PDFs) of the characteristic streak lift angles θ_c collected in each simulation. The solid black line is the average angle. The decrease of the average angle with increasing of Wi shows the weakening of the streak lift-up "strength", which indicates higher streak stability and less probability for vortex generation by streak instability. In addition, the shape of the distribution changes drastically from LDR to HDR. Before the LDR-HDR transition, the distribution is highly skewed with only
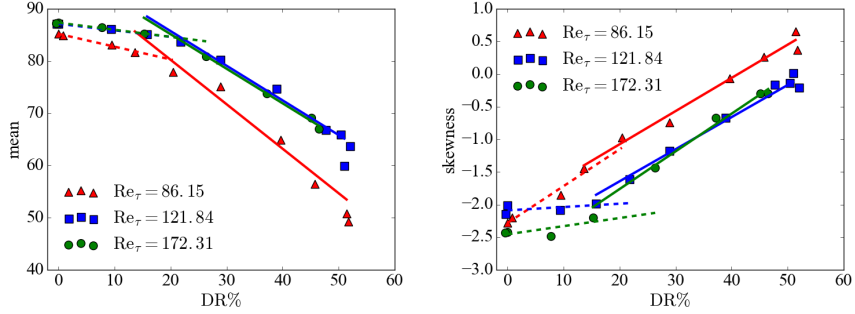
38

Figure 25: The mean and skewness of the θ_c distribution for all three Re_τ. The dashed and solid lines are the linear regression outcomes of the LDR and HDR stages, respectively.

one sharp peak located in the range of 80 and 90 degrees. As Wi increases, the
distribution of θ_c starts to spread towards the side of lower θ_c. At HDR, the distribution becomes nearly even for a wide range of θ_c with no distinct peak at the high θ_c end. The mean and skewness of the distribution are plotted in Figure 25 against DR% and it is clear that both metrics change sharply at the LDR-HDR transition (DR% $\approx$ 20%) (The turn of trend in skewness is not as clear only at the lowest Re but it becomes sharp at higher ones). Note that a streak is considered unstable at $\theta_c > 50$ for sinuous streak instability [53]. The sharp change in the distribution at the beginning of HDR indicates a drastic decrease in the number of streaks eligible for instability, which supports the mechanism we propose: HDR is a stage where the streak-instability pathway for vortex regeneration is greatly suppressed, exposing the parent-offspring mechanism as the main pathway (Figure 21(b)). Since the latter is known to maintain the clustering and close interaction between vortices, this mechanism consistently explains the observed turbulence localization.

4. Conclusions

In this study, DNS simulation of viscoelastic turbulent channel flow is performed for a large number of parameter combinations at a moderate-Re regime not far above Re_{crit}. The landscape of the Re-Wi parameter space is explored

39

(Figure 5), including the whole range of transitions in DR behaviors. In particular, we focus on the LDR-HDR transition, which occurs between the DR onset and MDR. Literature in the area often attributes the transition to a quantitative effect of the DR%. However, we show that it is indeed a qualitative transition of different turbulent dynamics.

Changes in flow statistics are first investigated and the major features of HDR (compared with LDR) are summarized as follows.

- The mean velocity profile deviates from the PvK log law behavior in the log-law layer (Figure 6).

- The Reynolds shear stress is suppressed not only in the buffer layer, but across the whole channel (except the viscous sublayer) (Figure 7).

- As the Reynolds shear stress becomes suppressed in the log-law layer, viscous and polymer shear stresses increases (Figure 9; in LDR, these changes only occur in the buffer layer).

- The energy spectrum in the log-law layer becomes qualitatively changed in the log-law layer, with a sudden increase in the energy accumulated in large scales (Figures 10 and 11).

In summary, unlike at LDR where most DR effects are contained in the buffer layer, at HDR these effects extend to the log-law layer. Behind these apparent changes in flow statistics, the turbulent structure has also changed fundamentally. At LDR, turbulent vortices homogeneously spread across the domain, but at HDR they cluster into strongly interacting groups. Turbulence becomes localized, leaving the regions outside these vortex clusters laminar-like. Percolation analysis reveals a fundamentally changed vortex topology at HDR (Figure 20).

These changes indicate that DR goes through two distinct stages with different mechanisms. The first starts at the onset of DR, where the coil-stretch transition of polymers starts a generic inhibition of all turbulent fluctuations.

40

The second mechanism is triggered at the LDR-HDR transition and its origin is unknown, for which a mechanism is proposed. In Newtonian turbulence, vortex regeneration cycles include two parallel pathways. The streak-instability pathway generates new vortices by perturbing streamwise low-speed streaks and the growth and lift-up of these vortices eventually lead to their bursting, which generates small-scale fluctuates that can destabilize another streak. This process is intrinsically non-local, as the perturbations can spread quickly to other parts of the domain, and the bursting events can feed the turbulence in the log-law layer. The parent-offspring pathway generates new vortices immediately next to an existing one. The vortices are thus clustered and interact strongly with one another. Polymers, for its capability of suppressing bursting and stabilizing streamwise vortices, are able to substantially block the first pathway, leaving the parent-offspring pathway the main mechanism of turbulence self-sustenance at HDR. The proposed mechanism offers a consistent explanation for the changes in flow statistics at the LDR-HDR transition and the localization of turbulence. Quantitative analysis of streak stability shows that after the LDR-HDR transition, much fewer streaks are susceptible to instability, which supports the mechanism.

Admittedly, the binary categorization of vortex regeneration mechanisms is simplistic and, more importantly, there still lacks sufficient direct evidence for the proposed mechanism. The nature of HDR is far from being a solved problem. For future work, we will further test this hypothesis by systematically investigating the polymer effects on the vortex regeneration process. This is difficult to achieve using DNS in statistically steady turbulence (as in this study), where the chaotic dynamics makes any direct comparison of vortex dynamics nearly impossible. Transient processes must be carefully constructed to simulate the vortex generation and growth dynamics. Results from different Wi can then be systematically compared for complete understanding. In the case of streak breakdown, examples of such transient processes can be borrowed from the existing literature on the Newtonian bypass transition [56]. In particular, recent work by Brandt and de Lange [65] offers a neat example of creating

41

different vortex configurations from controlled collisions between streaks. In addition, conditional sampling also offers a convenient way of generating hairpin vortices [66].

References

[1] Virk PS. Drag reduction fundamentals. AIChE J 1975;21(4):625–56.

[2] White CM, Mungal MG. Mechanics and prediction of turbulent drag reduction with polymer additives. Annu Rev Fluid Mech 2008;40:235–56.

[3] Graham MD. Drag reduction and the dynamics of turbulence in simple and complex fluids. Phys Fluids 2014;26:101301. doi:{10.1063/1.4895780}.

[4] Kim J, Moin P, Moser R. Turbulence statistics in fully-developed channel flow at low Reynolds-number. J Fluid Mech 1987;177:133–66.

[5] Housiadas KD, Beris AN. Polymer-induced drag reduction: effects of variations in elasticity and inertia in turbulent viscoelastic channel flow. Phys Fluids 2003;15:2369–84.

[6] Li W, Xi L, Graham MD. Nonlinear travelling waves as a framework for understanding turbulent drag reduction. J Fluid Mech 2006;565:353–62.

[7] Xi L, Graham MD. Turbulent drag reduction and multistage transitions in viscoelastic minimal flow units. J Fluid Mech 2010;647:421–52. doi:`10.1017/S0022112010000066`.

[8] Li CF, Sureshkumar R, Khomami B. Simple framework for understanding the universality of the maximum drag reduction asymptote in turbulent flow of polymer solutions. Phys Rev E 2015;92:043014. doi:`10.1103/PhysRevE.92.043014`.

[9] Pope SB. Turbulent flows. Cambridge, United Kingdom: Cambridge University Press; 2000. ISBN 0-521-59125-2.

[10] Warholic MD, Massah H, Hanratty TJ. Influence of drag-reducing polymers on turbulence: effects of reynolds number, concentration and mixing. Exp Fluids 1999;27(5):461–72.

[11] Ptasinski PK, Boersma BJ, Nieuwstadt FTM, Hulsen MA, den Brule BHAAV, Hunt JCR. Turbulent channel flow near maximum drag reduction: simulations, experiments and mechanisms. J Fluid Mech 2003;490:251–91.

[12] Min T, Choi H, Yoo JY. Maximum drag reduction in a turbulent channel flow by polymer additives. J Fluid Mech 2003;492:91–100.

[13] Li CF, Sureshkumar R, Khomami B. Influence of rheological parameters on polymer induced turbulent drag reduction. J Non-Newton Fluid Mech 2006;140(1):23–40.

[14] White CM, Dubief Y, Klewicki J. Re-examining the logarithmic dependence of the mean velocity distribution in polymer drag reduced wall-bounded flow. Phys Fluids 2012;24(2):021701.

43

[15] Deng BQ, Huang WX, Xu CX. Origin of effectiveness degradation in active drag reduction control of turbulent channel flow at $Re_\tau = 1000$. J Turbul 2016;17:758–86. doi:10.1080/14685248.2016.1181266.

[16] Lumley JL. Drag reduction by additives. Annu Rev Fluid Mech 1969;1:367–84. doi:10.1146/annurev.fl.01.010169.002055.

[17] De Gennes PG. Introduction to polymer dynamics. Cambridge, United Kindom: Cambridge University Press; 1990.

[18] De Angelis E, Casciola CM, Piva R. DNS of wall turbulence: dilute polymers and self-sustaining mechanisms. Comput Fluids 2002;31:495–507.

[19] Dubief Y, Terrapon VE, White CM, E. S. Shaqfeh PM, Lele SK. New answers on the interaction between polymers and vortices in turbulent flows. Flow Turbul Combust 2005;74(4):311–29.

[20] Li W, Graham MD. Polymer induced drag reduction in exact coherent structures of plane Poiseuille flow. Phys Fluids 2007;19:083101.

[21] Kim K, Li CF, Sureshkumar R, Balachandar S, Adrian RJ. Effects of polymer stresses on eddy structures in drag-reduced turbulent channel flow. J Fluid Mech 2007;584:281–99. doi:10.1017/S0022112007006611.

[22] Xi L, Graham MD. Active and hibernating turbulence in minimal channel flow of Newtonian and polymeric fluids. Phys Rev Lett 2010;104:218301. doi:10.1103/PhysRevLett.104.218301.

[23] Whalley RD, Park JS, Kushwaha A, Dennis DJC, Graham MD, Poole RJ. Low-drag events in transitional wall-bounded turbulence. Phys Rev Fluids 2017;2:034602. doi:10.1103/PhysRevFluids.2.034602.

[24] Xi L, Graham MD. Dynamics on the laminar-turbulent boundary and the origin of the maximum drag reduction asymptote. Phys Rev Lett 2012;108(2):028301.

44

[25] Xi L, Bai X. Marginal turbulent state of viscoelastic fluids: A polymer drag reduction perspective. Phys Rev E 2016;93. doi:{`10.1103/PhysRevE.93.043118`}.

[26] Wang SN, Shekarn A, Graham MD. Spatiotemporal dynamics of viscoelastic turbulence in transitional channel flow. J Non-Newton Fluid Mech 2017;.

[27] Xi L, Graham MD. Intermittent dynamics of turbulence hibernation in newtonian and viscoelastic minimal channel flows. J Fluid Mech 2012;693:433–72.

[28] Sureshkumar R, Beris AN, Handler RA. Direct numerical simulation of the turbulent channel flow of a polymer solution. Physics of Fluids 1997;9(3):743–55.

[29] Bird RB, Hassager O, Armstrong RC, Crurtis CF. Dynamics of polymeric liquids. Vol. 2 Kinetic Theory. John Wiley and Sons Inc., New York, NY; 1987.

[30] Peyret R. Spectral methods for incompressible viscous flow. 2002.

[31] Sureshkumar R, Beris AN. Effect of artificial stress diffusivity on the stability of numerical calculations and the flow dynamics of time-dependent viscoelastic flows. J Non-Newton Fluid Mech 1995;60:53–80. doi:`10.1016/0377-0257(95)01377-8`.

[32] Dimitropoulos CD, Sureshkumar R, Beris AN. Direct numerical simulation of viscoelastic turbulent channel flow exhibiting drag reduction: effect of the variation of rheological parameters. J Non-Newton Fluid Mech 1998;79:433–68.

[33] Gibson JF. Channelflow: a spectral navier–stokes simulator in c++. New Hampshire 2012;.

45

[34] Tuckerman LS, Kreilos T, Schrobsdorff H, Schneider TM, Gibson JF. Turbulent-laminar patterns in plane Poiseuille flow. Phys Fluids 2014;26. doi:{10.1063/1.4900874}.

[35] Nishioka M, Asai M. Some observations of the subcritical transition in plane poiseuille flow. J Fluid Mech 1985;150:441–50.

[36] Samanta G, Housiadas KD, Handler RA, Beris AN. Effects of viscoelasticity on the probability density functions in turbulent channel flow. Phys Fluids 2009;21:115106.

[37] Housiadas KD, Beris AN. On the skin friction coefficient in viscoelastic wall-bounded flows. Int J Heat Fluid Flow 2013;42:49–67.

[38] Owolabi BE, Dennis DJC, Poole RJ. Turbulent drag reduction by polymer additives in parallel-shear flows. J Fluid Mech 2017;453:57–108.

[39] Wei T, Willmarth WW. Reynolds-number effects on the structure of a turbulent channel flow. J Fluid Mech 1989;204:57–95.

[40] Kawamura H, Abe H, Matsuo Y. Dns of turbulent heat transfer in channel flow with respect to reynolds and prandtl number effects. Int J Heat Fluid Flow 1999;20(3):196–207.

[41] Housiadas KD, Beris AN. Polymer-induced drag reduction: Effects of the variations in elasticity and inertia in turbulent viscoelastic channel flow. Physics of Fluids 2003;15(8):2369–84.

[42] De Angelis E, Casciola CM, L'vov VS, Piva R, Procaccia I. Drag reduction by polymers in turbulent channel flows: energy redistribution between invariant empirical modes. Phys Rev E 2003;67:056312.

[43] Housiadas KD, Beris AN, Handler RA. Viscoelastic effects on higher order statistics and on coherent structures in turbulent channel flow. Phys Fluids 2005;17:035106.

[44] Robinson SK. Coherent motions in the turbulent boundary layer. Annu Rev Fluid Mech 1991;23(1):601–39.

[45] Warholic MD, Heist DK, Katcher M, Hanratty TJ. A study with particles image velocimetry of the influence of drag-reducing polymers on the structure of turbulence. Exp Fluids 2001;31:474–83.

[46] White CM, Somandepalli VSR, Mungal MG. The turbulence structure of drag-reduced boundary layer flow. Exp Fluids 2004;36:62–9.

[47] Jeong J, Hussain F. On the identification of a vortex. J Fluid Mech 1995;285:69–94.

[48] Dubief Y, Delcayre F. On coherent-vortex identification in turbulence. J Turbul 2000;1:1–22.

[49] Zhou J, Adrian RJ, Balachandar S, Kendall TM. Mechanisms for generating coherent packets of hairpin vortices in channel flow. J Fluid Mech 1999;387:353–96.

[50] Adrian RJ. Hairpin vortex organization in wall turbulence a. Phys Fluids 2007;19(4):041301.

[51] Boots BN, Getis A. Point pattern analysis; vol. 8. Sage Publications, Inc; 1988.

[52] Lozano-Durán A, Flores O, Jiménez J. The three-dimensional structure of momentum transfer in turbulent channels. J Fluid Mech 2012;694:100–30.

[53] Schoppa W, Hussain F. Coherent structure generation in near-wall turbulence. J Fluid Mech 2002;453:57–108.

[54] Hamilton JM, Kim J, Waleffe F. Regeneration mechanisms of near-wall turbulence structures. J Fluid Mech 1995;287:317–48.

[55] Brandt L, Henningson DS. Transition of streamwise streaks in zero-pressure-gradient boundary layers. J Fluid Mech 2002;472:229–61. doi:10.1017/S0022112002002331.

[56] Schlatter P, Brandt L, de lange HC, Henningson DS. On streak breakdown in bypass transition. Phys Fluids 2008;20:101505. doi:10.1063/1.3005836.

[57] Bai X, Xi L. Effects of drag-reducing polymers on turbulence growth and bursting in a near minimal channel 2017;Submitted.

[58] Yarin AL. On the mechanism of turbulent drag reduction in dilute polymer solutions: dynamics of vortex filaments. J Non-Newton Fluid Mech 1997;69(2-3):137–53.

[59] Kim K, Adrian RJ, Balachandar S, Sureshkumar R. Dynamics of hairpin vortices and polymer-induced turbulent drag reduction. Phys Rev Lett 2008;100(13):134504.

[60] Kim K, Li CF, Sureshkumar R, Balachandar S, Adrian RJ. Effects of polymer stresses on eddy structures in drag-reduced turbulent channel flow. J Fluid Mech 2007;584:281–99.

[61] Brooke JW, Hanratty TJ. Origin of turbulence-producing eddies in a channel flow. Phys Fluids A-Fluid 1993;5(4):1011–22.

[62] Miyake Y, Ushiro R, Morikawa T. The regeneration of quasi-streamwise vortices in the near-wall region. JSME International Journal Series B Fluids and Thermal Engineering 1997;40(2):257–64.

[63] Graham MD. Drag reduction in turbulent flow of polymer solutions. Rheol Rev 2004;2(2):143–70.

[64] Li CF, Sureshkumar R, Khomami B. Simple framework for understanding the universality of the maximum drag reduction asymptote in turbulent flow of polymer solutions. Phys Rev E 2015;92(4):043014.

[65] Brandt L, de Lange HC. Streak interactions and breakdown in boundary layer flows. Phys Fluids 2008;20:024107. doi:10.1063/1.2838594.

[66] Kim K, Adrian RJ, Balachandar S, Sureshkumar R. Dynamics of hairpin vortices and polymer-induced turbulent drag reduction. Phys Rev Lett 2008;100:134504. doi:10.1103/PhysRevLett.100.134504.

49